processes

MDPI

Article

Colloidal TiO_2 Nanorod Films Deposited Using the MAPLE Technique: Role of the Organic Capping and Absence of Characteristic Surface Patterns

Maura Cesaria [1,*], Antonietta Taurino [2,*], Pantaleo Davide Cozzoli [1], Valentina Arima [3] and Anna Paola Caricato [1]

[1] Department of Mathematics and Physics "Ennio De Giorgi", University of Salento, Via Arnesano, I-73100 Lecce, Italy; davide.cozzoli@unisalento.it (P.D.C.); annapaola.caricato@unisalento.it (A.P.C.)
[2] Institute for Microelectronics and Microsystems, IMM-CNR, Via Monteroni, I-73100 Lecce, Italy
[3] CNR NANOTEC Institute of Nanotechnology, c/o Campus Ecotekne, University of Salento, Via Monteroni, I-73100 Lecce, Italy; valentina.arima@nanotec.cnr.it
* Correspondence: maura.cesaria@unisalento.it (M.C.); antonietta.taurino@cnr.it (A.T.)

Abstract: Thin films of titanium dioxide (TiO_2) nanocrystals, widely acknowledged for their unique physical-chemical properties and functionalities, are used in disparate technological fields, including photovoltaics, sensing, environmental remediation and energy storage. In this paper, the preparation of thin films consisting of anatase-phase TiO_2 nanorods deposited using the matrix-assisted pulsed laser evaporation (MAPLE) technique and their characterization in terms of morphology, elemental composition and wettability are presented and discussed. Particular attention is paid to the effects of the laser fluence, varied over a broad range (F = 25, 50, 100 mJ/cm^2), and to the role of the capping surfactants bound to the surface of the nanorod precursors. Whereas increasing fluence favored a partial removal of the surface-bound surfactants, a post-growth UV-light-driven photocatalytic treatment of the films was found to be necessary to reduce the incorporated fraction of organics to a further substantial extent. It was noteworthy that, under our experimental conditions, the distinctive surface patterns and roughness that commonly degrade the morphology of films deposited using the MAPLE technique were not observable. This previously unreported experimental evidence was rationalized on the basis of the interaction dynamics between solvent/solute droplets ejected from the laser-irradiated target and the rough surfaces of the growing film.

Keywords: thin films; TiO_2 nanorods; organic capping; MAPLE technique; laser fluence; elemental/morphological analyses; photocatalytic degradation; missing MAPLE surface patterns

check for updates

Citation: Cesaria, M.; Taurino, A.; Cozzoli, P.D.; Arima, V.; Caricato, A.P. Colloidal TiO_2 Nanorod Films Deposited Using the MAPLE Technique: Role of the Organic Capping and Absence of Characteristic Surface Patterns. *Processes* **2023**, *11*, 2591. https://doi.org/10.3390/pr11092591

Academic Editors: Zois Syrgiannis and Wang Chuanyi

Received: 26 June 2023
Revised: 19 August 2023
Accepted: 27 August 2023
Published: 29 August 2023

1. Introduction

Since its commercial production in the early twentieth century, titanium dioxide (TiO_2) polymorphs have been used in a plethora of applicative fields, such as in the realization of optical and spintronic devices, ultra-thin capacitors, filters, power circuits, temperature-compensating condensers, resistive random access memories, photovoltaics, photocatalysts for environmental decontamination and viral disinfection, self-cleaning protective coatings, switchable superhydrophobic-to-super-hydrophilic surfaces, photo/electrochromic windows and sensors, as well as in the formulation of pigments, plastics, paints, ceramics, cosmetics, bone-implants and additives for the food industry [1–9]. Such high versatility of the semiconductor TiO_2 stems from its unique photophysical and physical-chemical properties: a high refractive index and dielectric constant, large band-gap (3.0–3.2 eV), excellent visible and near-infrared transmittance, chemical and thermal stability, photo-durability, mechanical robustness, biocompatibility and high performance as a photocatalyst for water splitting and degradation of organics under ultraviolet light [3,7,10–12].

Nanostructured TiO_2 films (e.g., consisting of nanoparticles, nanotubes, nanorods, nanoflowers and other shape-controlled nanocrystals) have received considerable attention due to the far higher surface-to-volume ratio of their constituent nanoscale building blocks with respect to the bulk phase, allowing the enhancement of the inherent surface photo-reactivity of the material [12–15]. However, since the confinement of carriers in nanosized crystals may lead to an increased probability of undesired electron–hole recombination, photocatalytic activity can be further improved by using anisotropic-shaped nanostructures, such as nanorods, nanowires, nanotubes or branched nanocrystals, in place of their spherical counterparts, to allow a more effective carrier delocalization (after exciton dissociation) along the less-confined dimension(s).

Concerning the most common TiO_2 polymorphs, (i) rutile is the most thermodynamically stable phase in the temperature range 600–1855 °C; (ii) the anatase and brookite polymorphs are metastable, but can be kinetically preferred under ordinary synthesis conditions at temperatures below ~400 °C; (iii) the transition from anatase and brookite to rutile can be driven post-synthesis by heating, depending on the nanocrystal size [6,16,17]. In regard to the photocatalytic activity, anatase is more active than rutile and dominant in the nanoscale regime because of its lower surface energy [18]. However, high photocatalytic activity was also observed when coupling the anatase and rutile phases in such a way that the relative staggering of the conduction-band edges favored selective transfer of excited electrons from anatase to rutile, thus suppressing exciton recombination [19].

Approaches mostly used to fabricate TiO_2 nanoparticles include both wet-chemical and vacuum-based physical techniques, such as metalorganic chemical vapor deposition (MOCVD) [20], pulsed chemical vapor deposition [21], reactive magnetron sputtering [22], colloidal routes based on sol–gel chemistry [23] and thermal hydrolysis reactions [24], filtered cathodic vacuum arc discharge [25], nanodot-assisted hydrothermal growth [26] and pulsed-laser-based deposition (PLD) [27,28]. Physical techniques are optimal to control the compositional purity of nanoparticles; however, they can be time-consuming, involve complex chemical processes and are frequently based on the use of toxic chemical precursors (gases), which ultimately leads to low product yield and poor control over the size variance of the nanoparticles. On the other hand, crystalline nanoparticles with well-tailored size and shape distributions can be synthesized using solution-based chemical routes, which are relatively cheap and easy to implement [29], but may be affected by the presence of contaminants (impurities in the reagents and/or solvents). Among them, organic-assisted synthetic methods, which rely on the judicious use of surface-coordinating agents (e.g., organic ligands, surfactants) to control the fundamental nucleation and growth stages and inhibit aggregation, have been distinguished for their capability to produce highly monodisperse size- and shape-controlled nanocrystals through careful regulation of the synthesis parameters. The as-derived solution free-standing nanostructures can be further manipulated and processed to serve as building blocks for the fabrication of functional thin films for processes and devices using simple and low-cost deposition techniques, such as spin-coating and drop-casting, or guided self-assembly. Such approaches, however, do not guarantee the formation of extended nanocrystal-based films with adjustable thickness, porosity and uniform surface coverage of the underlying substrate, particularly over rough surfaces [17]. Therefore, there is still much scope in the development of reproducible and reliable deposition methods for obtaining thin films with controllable quality features for targeted applications.

The MAPLE (matrix-assisted pulsed laser evaporation) technique, developed in the late 1990s at the U.S. Naval Research Laboratory for the deposition of functional organic materials in the chemical sensing field [30], represents a very attractive contamination-free alternative approach to deposit preformed nanoparticles/nanocrystals into high-quality

films on different types of substrate, including thermally sensitive, patterned and non-planar substrates [17]. The MAPLE technique was originally designed to provide a gentle laser-based approach for transferring simple polymers, polymer blends and general photo- and thermal-sensitive biomaterials with minimal damage [30].

In particular, the MAPLE-based deposition of nanostructure-based thin films is accomplished by utilizing, as the starting film precursors, colloidal solutions or stable suspensions of the desired organic-capped nanostructures, dispersed in a volatile, laser-absorbing solvent at a concentration of a few weight percentages [17]. Such a precursor solution is then frozen at the liquid N_2 temperature to serve as the MAPLE target to be irradiated [30] using ultraviolet (UV) or infra-red laser sources [31]. Under conditions of poor or no absorption by the solute at the laser wavelength and no photochemical interaction between solvent and solute, the laser energy mainly absorbed by the solvent drives the ejection of the solute molecules from the frozen target with minimal photothermal and photochemical decomposition. The target-to-substrate transport of the solute occurs within the expanding plasma plume (Figure 1). The MAPLE technique has been demonstrated to be a versatile and successful approach to deposit pure and functionalized/doped titania nanostructures [32–35].

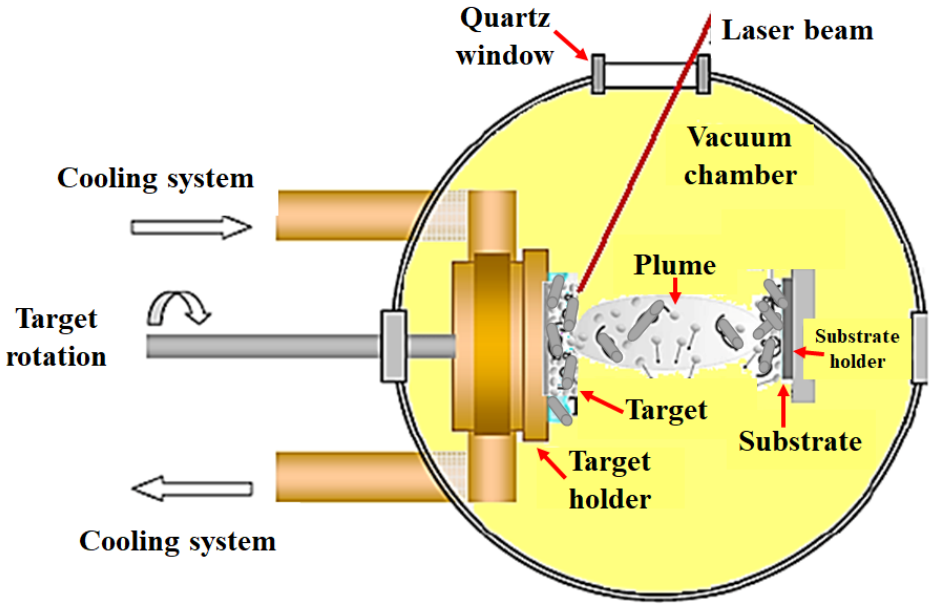

Figure 1. Sketch of a typical experimental set-up used in MAPLE experiments using a precursor colloidal solution to deposit nanoparticle films.

As is known, the physical and chemical properties, as well as the functional capabilities of colloidal TiO_2-based thin films, are highly correlated with the crystal phase, geometry (size and shape), types and surface distribution of exposed facets of their nanocrystal building blocks [36].

The capping molecules (typically surfactants), which are used to control crystal evolution in liquid media and remain bound to the as-grown colloidal TiO_2 nanocrystals after the synthesis, affect their surface properties (e.g., wettability, chemical reactivity), thus governing their solubility and interaction with the environment. Depending on the specific technological purposes, such organic capping ligands may be exchanged for other types of molecules, or may be removed/degraded upon application of thermal or UV-light treatments [37,38]. As MAPLE depositions involve UV-laser irradiation of surfactant-capped TiO_2 nanostructures, it is worth investigating whether UV-laser irradiation may affect the

native capping ligands anchored to the nanocrystals during the explosive boiling mechanism, and if so, to what extent. Indeed, the surface features, including residuals of the synthesis surfactants, of the final deposited nanocrystals have to be taken into account when designing post-growth treatments and specific applications.

In addition, another uninvestigated aspect is how the presence of capping molecules may impact on the microstructural and morphological characteristics of the MAPLE-deposited TiO_2 nanocrystal films, given the expected complex evaporative patterns characteristic of the MAPLE technique [39,40], and the modified dynamics of solvent evaporation in the case of solutions including colloids and soft matter [41].

In this study, thin films of colloidal anatase-phase TiO_2 nanorods (TiO_2 NRs) deposited using the MAPLE technique were characterized in terms of their morphology, elemental composition and wettability to gain knowledge and understanding on the impact of relevant experimental parameters and conditions. In this respect, the role of the capping surfactants bound to the surface of the nanorod precursors and the influence of the laser fluence were considered in relation to possible thermally induced pathways of partial degradation or removal of the organic coating molecules. A post-growth UV-light-driven photocatalytic treatment of the films was found to be necessary to reduce the incorporated fraction of organics to a further substantial extent. It is noteworthy that under our deposition conditions, the characteristic surface patterns/morphologies (ring-like patterns, deflated balloons and solute aggregates) that degrade thin films fabricated using the MAPLE technique were absent. This previously unreported, to the best of our knowledge, experimental evidence is discussed in terms of the interaction dynamics between the solvent/solute droplets ejected from the laser-irradiated target and the surfaces of the growing film that are highly inhomogeneous and rough due to the presence of the organic capping on the TiO_2 NRs.

The purpose of the study was to gain a deeper knowledge and understanding of the impact of relevant experimental parameters and conditions in such a way to develop an experimental protocol yielding organic capping-free and high-quality nanostructured TiO_2 films deposited using the MAPLE technique. In particular, the morphological evolution of MAPLE-deposited OLAC/OLAM-capped TiO_2 NR-films versus fluence conditions, which account for heating-induced effects, and applied UV treatments, which account for photochemical effects, are thoroughly discussed.

2. Materials and Methods

2.1. Synthesis of Colloidal TiO_2 Nanorods

2.1.1. Materials

All chemicals were of the highest purity available and were used as received. Titanium tetraisopropoxide ($Ti(OPr^i)_4$ or TTIP, 97%), titanium tetrachloride ($TiCl_4$, 99.999%), trimethylamine *N*-oxide dihydrate ($(CH_3)_3NO{\cdot}2H_2O$ or TMAO, 98%), oleic acid ($C_{17}H_{33}CO_2H$ or OLAC, 90%), 1-octadecene ($C_{17}H_{36}$ ODE, 90%) and oleyl amine ($C_{17}H_{33}NH_2$ or OLAM, 70%) were purchased from Aldrich. All solvents were of analytical grade and were also purchased from Aldrich.

2.1.2. Synthesis Procedure

Colloidal TiO_2 nanorods (NRs) with average diameter of ~3–4 nm and length of ~15 nm were prepared by reacting TTIP (15 mmol) with an aqueous trimethylamine *N*-oxide solution (2 M) in OLAC (70 g) at 100 °C for 70 h [42]. Longer NRs with mean diameter of ~3–4 nm and length of ~40 nm were prepared by reacting $TiCl_4$ (2 mmol) with OLAM (25 mmol) and OLAC (2 mmol) in ODE (6 g) at 280 °C for 45 min under nitrogen (N_2) atmosphere [43]. After the standard extraction and purification procedures (which included TiO_2 flocculation induced using alcohol addition to the crude reaction mixture, centrifugation, separation and washing of the TiO_2 precipitate), the as-obtained NRs were dispersible in non-polar media (such as toluene or chloroform) to yield optically clear solutions or stable

suspensions, depending on their dimensions and on the concentration realized. For the purposes of the present work, two TiO_2 stock precursor solutions in toluene were prepared, one containing the 3–4 nm × 15 nm NRs at a concentration of 5.0 wt% and one containing the 3–4 nm × 40 nm NRs at a concentration of 0.9 wt%, respectively. The stock solutions were stored at room temperature before further use.

2.2. MAPLE Deposition Experiments

The typical MAPLE deposition set-up used in our experiments is sketched in Figure 1. It consisted of (i) a pulsed laser beam source; (ii) a deposition vacuum chamber with a cryogenic target holder capable of hosting a target frozen at the liquid nitrogen (N_2) temperature during the deposition; (iii) a pumping system to maintain a suitable vacuum level as well as suckle the solvent away during the plasma plume expansion following ablation; and (iv) a substrate to collect the ablated species. In an idealized picture of a MAPLE experiment [44], a frozen target, consisting of the precursor material, which is intended to be deposited, dissolved/suspended in a volatile light-absorbing solvent, is irradiated using a pulsed laser with proper fluence conditions to cause an explosive-like collective ejection of material. Then, the formation of a plasma plume transfers the solute onto the substrate surface, where the deposited species arrange depending on kinetic energy conditions and substrate properties.

In our MAPLE deposition experiments, the TiO_2 stock precursor solution was first ultrasonicated for 10 min to disrupt any possible microaggregates formed during storage, then it was frozen at the liquid N_2 temperature to serve as the MAPLE target. The latter was finally introduced into the high-vacuum chamber at a background pressure of 10^{-4} Pa, fixed onto a rotating (3 Hz) holder to allow uniform erosion under laser irradiation and continuously cooled with liquid N_2 to maintain a constant temperature (−160 °C). The substrate was placed in front of the target at a distance of 45 mm. A KrF excimer laser beam (Lambda Physik LPX-305i, Goettingen, Germany), operating at a wavelength of 248 nm with a pulse duration of 20 ns and repetition rate of 10 Hz, was incident on the target at 45 degrees with respect to the normal target plane. Before starting the MAPLE deposition, the frozen water vapor overlying the target surface was removed by firing a few hundred laser pulses while a shutter screened the substrate. Relevant laser parameters, that is the fluence (F) and the number of laser pulses (N_p), were set as detailed in Table 1: fluence was varied from 25 to 100 mJ/cm^2 and N_p was varied from 20,000 to 8000. Since an increase in fluence leads to higher deposition rate, the number of laser pulses was tuned to control film thickness. For a given TiO_2 NR length, films with comparable thickness can be obtained by calibrating the number of laser pulses at each set fluence. Such samples allowed us to study the possible correlation between the morphology of the films and their organic capping component.

Table 1. List of samples deposited using MAPLE and relevant experimental parameters (L, length of the TiO_2 NRs, F fluence and Np number of laser pulses). For each sample, the contact angle (CA) measured before and after the UV-irradiation treatment, briefly termed CA and CA_{UV}, respectively, is also reported (see paragraphs 2.5 and 3.4).

Sample	Length (nm)	F (mJ/cm^2)	N_p	WCA (°)	WCA_{UV} (°)
NR (15, 25/20,000)	15	25	20,000	137 ± 4	58 ± 6
NR (15, 50/15,000)	15	50	15,000	152 ± 5	42 ± 3
NR (15, 100/8000)	15	100	8000	103 ± 10	25 ± 9
NR (40, 50/15,000)	40	50	15,000	94 ± 2	56 ± 5
NR (40, 100/8000)	40	100	8000	94 ± 5	52 ± 6

Henceforth, the deposited thin-film samples are referred to using the notation NR (L, F/N_p), where L is the numerical value of average length (15 nm or 40 nm) of the TiO_2

NRs in the corresponding stock precursor solution; F = 25, 50, 100 mJ/cm^2; and Np = 20,000, 15,000, 8000 (Table 1). A total of 100 Si substrates or SiO_2 slabs were used as substrates to allow post-deposition physical-chemical characterization of the thin films using different investigative techniques.

2.3. Ultraviolet (UV) Light Irradiation Treatments

To remove the organic components associated with the TiO_2 NRs and modify the inherent wettability of their surfaces, the as-deposited thin films were subjected to prolonged ultraviolet (UV) illumination [14,45]. Experimental irradiation conditions were regulated on the basis of the results of previous studies on the photostability of OLAC and OLAM ligands on the surface of colloidal TiO_2 NRs, analogous to those utilized in the present work [37,46]. Two consecutive photocatalytic UV light irradiation treatments were applied using a continuous wave (cw) 150 W Xe lamp with emission set at approximately (254 ± 10) nm via appropriate UV-pass filters under ambient conditions (i.e., in air and at room temperature). The samples were placed at a distance from the light source, at which the impinging energy density was approximately 5 mW/cm^2.

In detail, the first UV treatment, henceforth denoted as UV(1), consisted of an irradiation period from 2 to 7 h; the second UV treatment, henceforth denoted as UV(2), involved an irradiation time of up to 14 h. When discussing the UV-irradiated samples, the label UV(i) will be used, where i = 0 refers to the UV-untreated sample and i = 1, 2 denotes the first (i = 1) or the second (i = 2) UV treatment applied to the film, respectively.

2.4. Morphological and Compositional Analyses

The morphological parameters (shape and size) of the as-synthesized colloidal TiO_2 NRs were inspected using transmission electron microscopy (TEM) images acquired with a Jeol Jem 1011 TEM microscope (JEOL company, Tokyo, Japan) operating at an accelerating voltage of 100 kV. The samples for TEM analyses were prepared by dropping a dilute solution of the NRs dispersed in toluene onto a standard carbon-coated copper grid and then allowing the solvent to evaporate. Subsequently, the grids were transferred to the TEM microscope.

The morphological and compositional properties of the as-deposited thin films were investigated using plan-view scanning electron microscopy (SEM) and energy-dispersive X-ray spectroscopy (EDS), respectively. In detail, a Zeiss NVISION 40 dual beam Focused Ion Beam (FIB) system equipped with a high-resolution SEM GEMINI column and an Inca Energy 350 X-ACT Oxford EDS spectrometer was used. FIB cross-sections were obtained and used to analyze the films' transversal section oriented at 54° with respect to the electron beam.

Notably, the systematic investigation of the properties of the pristine and UV-treated TiO_2 NRs have been discussed in great detail elsewhere [37,42,46], and this led to the conclusions that (i) the UV treatment impacts the degradation of the organic capping molecules without affecting the inorganic TiO_2 NR components, and (ii) the laser pulse TiO_2–NR interaction may be tuned to avoid phase and structural changes of the TiO_2 NRs [35,47,48]. Information gained in earlier experimental and characterization sessions is a well-established background to develop further studies. Herein, the focus is on the deposition process and, in particular, the concurrent effect of laser fluence and UV irradiation on the morphological evolution and properties of TiO_2 films. The aim was to gain an insight into how to achieve control in two aspects: removal of the organic capping contaminant and occurrence of the typical MAPLE surface artifacts that degrade the film's quality. Accordingly, the results of systematic SEM and EDS investigations, which provided information on the particle arrangement on the substrate after MAPLE transfer and UV irradiation, are reported.

2.5. Contact Angle Measurements

In order to investigate the wettability of the MAPLE-deposited TiO_2 NR-based films, experiments measuring the contact angle were carried out. Static water contact angles (WCA) were measured using the sessile drop method using a CAM 200 (KSV Instruments Ltd., Helsinki, Finland) instrument. The volume of the applied droplets of distilled water was 3 μL. The values of WCA reported in this work correspond to an average over four measurements performed in different parts of the sample surface and the error was calculated as their standard deviation.

2.6. Transmittance and Absorbance

Transmittance and diffuse reflectance spectra of the films under study were measured at normal light incidence by using a Varian Cary 500 UV–Vis–NIR double-beam spectrophotometer equipped with an integration sphere accessory. A carefully cleaned bare SiO_2 substrate was used as reference to measure the transmittance normalized with respect to the substrate. Diffuse reflectance spectra were also recorded with a Varian Cary 500 UV–Vis–NIR double-beam spectrophotometer equipped with an integration sphere accessory. Both transmittance (T) and reflectance (R) spectra were recorded over the 200–2500 nm spectral range with a spectral resolution of 3 nm. Absorbance (Abs) was calculated using the relationship $Abs = 1 - T - R$.

3. Results

3.1. TiO_2 Precursor Solutions

For the purposes of the present study, organic-capped anatase TiO_2 NRs with different geometric parameters were synthesized using established colloidal sol–gel routes, based on thermal processing of metalorganic molecular precursors in hot mixtures of selected surfactants, namely OLAC and OLAM, the latter serving as reactants, nanoparticle stabilizers and promoters of anisotropic growth [37,46]. The as-synthesized and purified NRs individually consisted of a rod-shaped crystalline TiO_2 lattice protected by a discontinuous organic shell of tightly surface-bound surfactant derivatives, depending on the specific reaction conditions. The OLAC-capped NRs, prepared using slow alkaline hydrolysis of titanium tetraisopropoxide in OLAC at 100 °C [42], were passivated using oleate anions (i.e., deprotonated OLAC molecules) anchored to the TiO_2 surfaces via their carboxylate heads [42]. On the other side, the OLAC + OLAM-capped NRs, produced using aminolysis of in situ formed titanium–oleate complexes in $TiCl_4$/OLAM/OLAC mixtures at 280 °C in an inert atmosphere, were enwrapped by a mixture of oleate anions and/or neutral OLAM molecules (with a larger fraction of OLAM relative to OLAC), the latter bound to the TiO_2 surfaces via their amine moieties [43]. In both cases, the capping ligands were arranged on the TiO_2 surfaces so as to expose their conformationally disordered alkyl chains outwards. Thus, the overall thickness of the capping shell could be expected to be of less than ~2 nm, the approximate length of an unbent OLAC or OLAM molecule. Owing to their stable inorganic-core/hydrophobic-coating core/shell configuration, the NRs could be dispersed in non-polar solvents, such as toluene, to yield readily processable homogeneous TiO_2 solutions or suspensions, utilizable as precursors for the MAPLE deposition of thin films. In Figure 2, representative low-magnification TEM images of the as-synthesized colloidal TiO_2 NRs demonstrated the formation of populations of distinct anisotropic-shaped NRs with negligible tendency to aggregate: the shortest OLAC-capped NRs [43] exhibited a projected rectangular-like profile with an average short- and long-axis size of ~3–4 nm and ~15 nm, respectively (Figure 2a); the largest NRs, protected by a mixed capping layer of OLAC and OLAM ligands (with a larger fraction of OLAM relative to OLAC) [44], featured a tip-tapered profile with an average short-axis size of ~3–4 nm and length of ~40 nm, respectively (Figure 2b). As reported previously [43,44], the NRs possessed a single crystalline anatase-phase (tetragonal) lattice elongated in the <001> direction; specifically, the NRs typically exposed crystallographically equivalent (011)/(101) facets along the stepped longitudinal sidewalls and (001) facets at the apexes. Further details on the morphological

structural and compositional characteristics of the synthesized TiO_2 NRs can be found elsewhere [42,43].

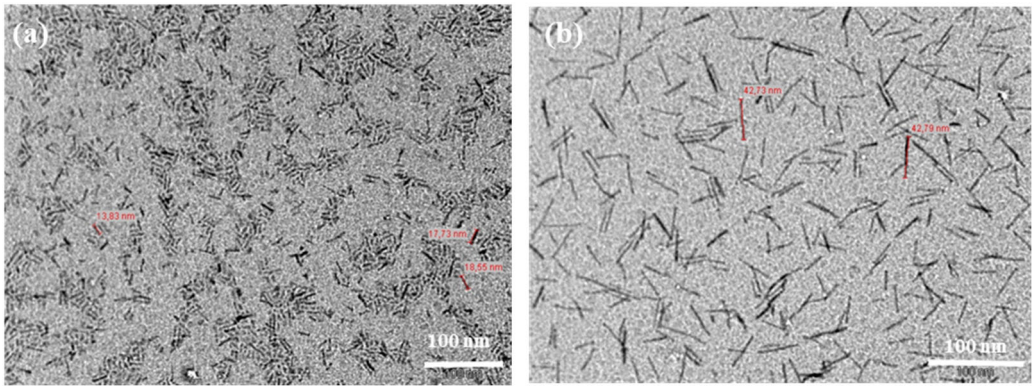

Figure 2. Low-resolution TEM images of the as-synthesized surfactant-capped anatase TiO_2 NRs: (**a**) ~3 nm × ~15 nm OLAC-capped NRs from stock solution NR (15, 5 wt%)); (**b**) ~3 nm × ~40 nm OLAC + OLAM-capped NRs from stock solution NR (40, 0.9 wt%).

3.2. As-Deposited TiO_2 NR Films: Morphology and Composition

Figure 3 reports low-magnification SEM plan view (Figure 3a,d,g), tilted view (Figure 3b,e,h) and FIB-prepared cross sections (Figure 3c,f,i) of samples NR (15, 25/20,000), NR (15, 50/15,000) and NR (15, 100/8000), which form a set of representative thin films deposited using the shorter OLAC-capped ~3–4 nm and ~15 nm TiO_2 NRs from the stock solution NR (15, 5 wt%). In general, the films showed an irregular and jagged surface morphology with shallow voids, deep holes and rounded irregular structures. The relevant information provided by the SEM investigation at this level was the presence of an organic matrix encasing the TiO_2 NRs. In particular, the lowest fluence corresponded to the highest roughness, resulting in the presence of voids and protrusions, which was also evident in the FIB cross sections, showing a very irregular film whose thickness varied as a result of the high roughness from a few tens of nanometer up to 300 nm. The roughness decreased with the increase in the fluence and at 100 mJ/cm^2 the obtained film showed an improved surface uniformity and film compactness, as well as a uniform thickness of approximately 800 nm, as measured by the FIB cross section. Notably, in this case the presence of nanostructures embedded in a matrix of a different material was observed on the sample surface (see Figure 3g). The highest roughness exhibited by sample NR (15, 25/20,000) was expected based on the interplay between the specific deposition conditions, that is, the low fluence (25 mJ/cm^2), which yields low surface diffusivity of the deposited species, and the high number of laser pulses (Np = 20,000), which favors the accumulation of the depositing nanocrystals, in competition with the kinetic energy-driven mobility.

As a consequence, the growing film was in a frozen-like state and the progressive solvent evaporation was expected to produce an increasing density and size of inner voids, thus leaving a porous and rough microstructure evident even by visual inspection of the SEM images. Hence, the increased laser fluence and decreased number of laser pulses were expected to promote hyperthermal surface mobility and effective solvent evaporation during the target-to-substrate transport phase, thus leading to more compact films with reduced roughness, in agreement with the results of our morphological inspections.

Figure 4 reports the SEM images, taken at different degrees of magnification, of samples NR (40, 100/8000) and NR (40, 50/15,000), with representative thin films deposited using the longer OLAC + OLAM-capped ~3–4 nm and ~40 nm TiO_2 NRs from the stock solution NR (40, 0.9 wt%). In this case, completely different surface features were observed, in particular this included reduced roughness and visibility of the pristine nanostructures that suggested reduced organic contamination. Figure 4a,b show the plan-view image of NR (40, 50/15,000), where the occurrence of rod-like nanostructures, with a length consistent with the expected one based on the precursor solution, and rounded nanoparticles, with

a diameter ranging from a few nm to almost 20–30 nm, was observed. As evident in Figure 4c,d, NR (40, 100/8000) exhibited a prevalence of spherical structures [35]. Both images were affected by a blurring effect on the image contrast of the nanostructures, suggesting the presence of organic contaminants which inhibited the visibility of the fine details of the particle's morphology.

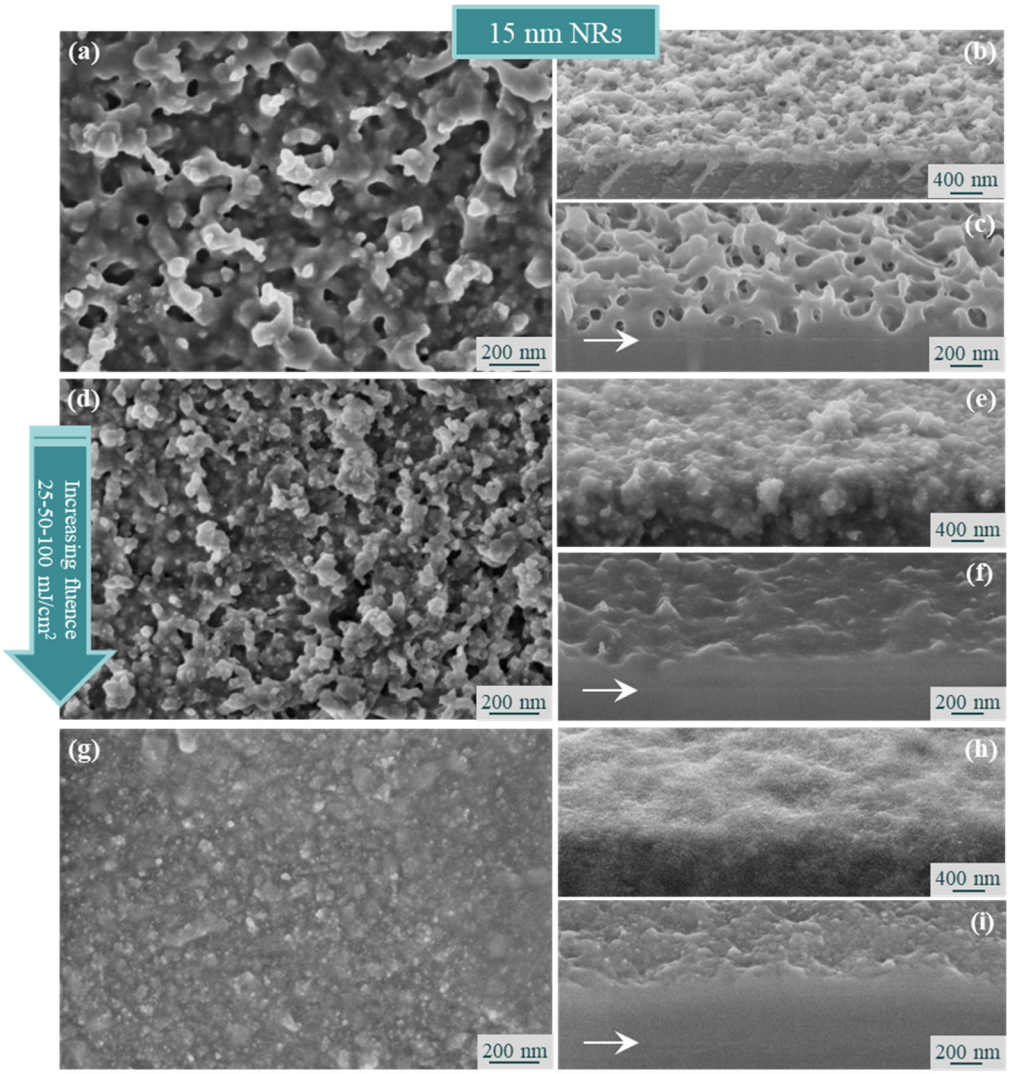

Figure 3. SEM plan view (**a**,**d**,**g**), tilted view (**b**,**e**,**h**) and FIB-prepared cross-sectional images (**c**,**f**,**i**) of the samples NR (15, 25/20,000), NR (15, 50/15,000) and NR (15, 100/8000) (from top to bottom, respectively).

In order to investigate the possible correlation between the observed morphology and the fluence-dependent composition in terms of the organic component (i.e., surfactant capping) associated with the starting OLAC-capped TiO_2 NRs, EDS analysis was carried out. In particular, for each sample EDS spectra were acquired and averaged over different regions with an extension of approximately 10^4 μm^2 to ensure their statistical significance. The typical EDS spectra reported in Figure 5a,b refer to samples NR (15, 100/8000) and NR (40, 100/8000). Four main peaks of interest, corresponding to the k_α lines of Ti (at 4.508 keV), Si (at 1.739 keV), O (at 0.525 keV) and C (at 0.277 keV), were detected.

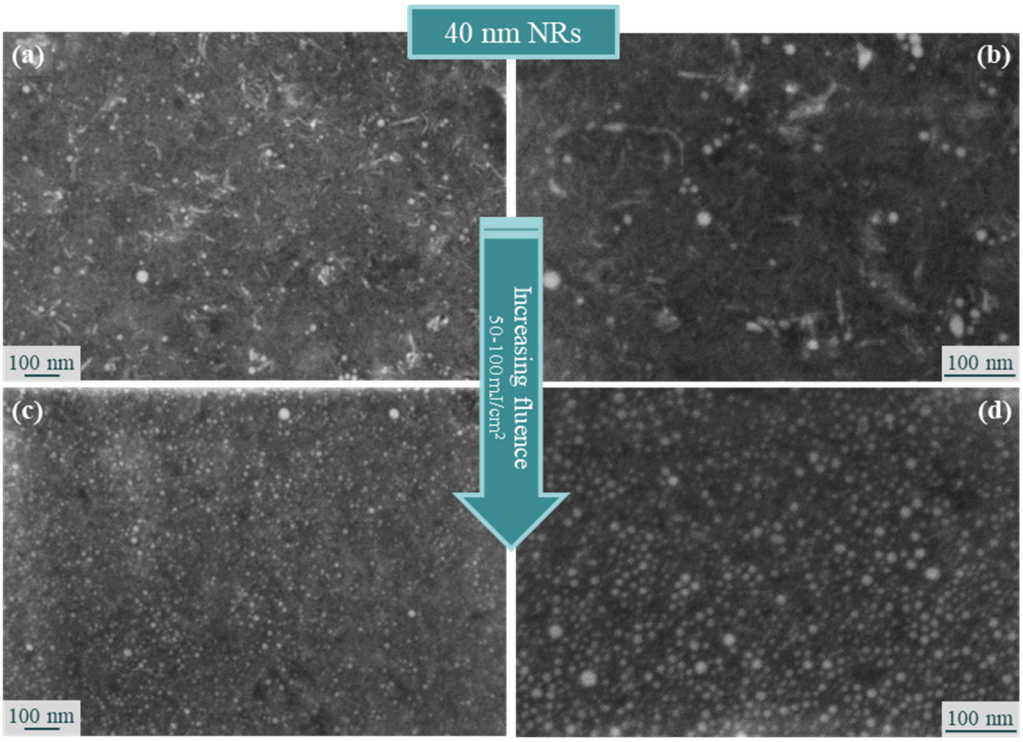

Figure 4. (**a**,**c**) Low- and (**b**,**d**) high-magnification SEM images of the samples (**a**,**b**) NR (40, 50/15,000) and (**c**,**d**) NR (40, 100/8000).

In order to obtain meaningful quantitative information on the different composition of the investigated samples, the count ratios of Ti/Si, Ti/O and Ti/C were estimated and compared using the main kα peaks. The graph in Figure 5c reports the count ratios, as derived from the EDS analyses of the samples including 15 nm long NRs, as a function of the laser fluence. It was observed that as the fluence increased from 25 to 100 mJ/cm^2, the Ti/Si peak ratio increased due to the growing contribution of Ti associated with increases in the thickness and compactness of the film, in agreement with the cross-sectional analysis. The signal associated with O and C supported the fact that the TiO_2 NRs were embedded using residual organics even at the highest fluence deposition. On the other side, the progressively increasing Ti/O and Ti/C ratios were indicative of the laser-aided removal of the original OLAC capping agents from the TiO_2 NR surface to an extent that scaled with the laser fluence. In the case of samples NR (40, 50/15,000) and NR (40, 100/8000), the EDS analyses shown in Figure 5d revealed that the Ti/O and Ti/C peak ratios were nearly insensitive to increases in the fluence. These results were consistent with the proportionally larger mass fraction of OLAC ligands associated with the shorter OLAC-capped ~3–4 nm and ~15 nm NRs, when compared to the larger OLAC + OLAM-capped ~3–4 nm and ~40 nm NRs.

Apart from the difference in the NR concentration of the precursor solutions NR (40, 0.9 wt%) and NR (15, 5 wt%), the lower percentage of OLAC surfactant used in combination with OLAM associated with the longest NRs reflected the lower impact of fluence on the removal/degradation of the organic surfactants. Definitively, the laser-target interaction did not result in the complete elimination of the capping surfactants, although increasing the laser fluence generally reduced the organic fraction of the films.

On the other hand, it is worth remarking that, in all the investigated samples, there was no evidence for the surface features commonly observed in films prepared using MAPLE that stem from transfer and collapse onto the substrate of polymer–solvent clusters, containing a mixture of liquid and vapor solvent molecules [40]. Indeed, unlike in the ideal solvent-free picture, MAPLE films can exhibit complex micrometer-sized surface features (such as collapsed pipes, elongated nanofibers, deflated balloons and ring-like evaporative

patterns) with characteristic sizes ranging from tens of nanometers to tens of microns due to residual solvent/solute mixtures. As a result, MAPLE films suffer from non-uniform substrate coverage and high roughness, requiring careful optimization of the experimental parameters [49].

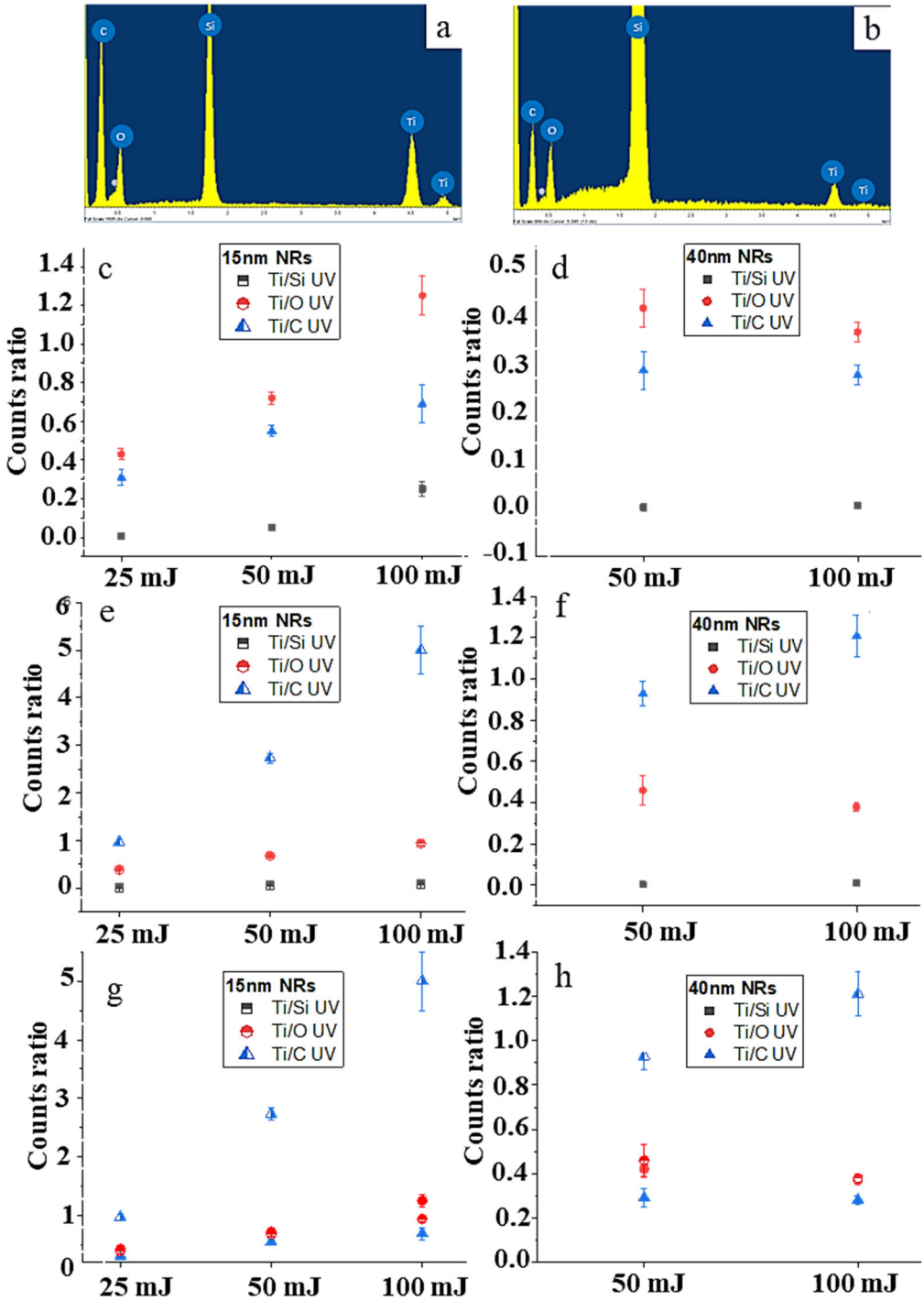

Figure 5. Representative EDS spectra of (**a**) NR (15, 100/8000) and (**b**) NR (40, 100/8000) showing four main peaks of interest associated with the kα lines of Ti (at 4.508 keV), Si (at 1.739 keV), O (at 0.525 keV) and C (at 0.277 keV). (**c**–**h**) Plots of the ratios Ti/Si, Ti/O and Ti/C as a function of the laser fluence of the samples consisting of 15 and 40 nm long TiO_2 NRs, before and after the UV treatment.

3.3. Effects of the UV Treatment

The organic capping molecules that passivated the surface of the as-synthesized TiO_2 NRs within the films were removed by stimulating the well-known photocatalytic degradation properties of TiO_2 using continuous band-gap excitation with ultraviolet (UV) light under ambient conditions (i.e., in the presence of atmospheric water and dioxygen, which are necessary participants in the fundamental reaction pathways across the photocatalytic cycle) [45]. The photocatalyzed removal of the hydrophobic surface-bound ligands, which typically requires several hours to proceed appreciably, was accompanied by photo-assisted hydroxylation of the TiO_2 surface due to photoinduced surface-adsorption of atmospheric H_2O molecules, eventually followed by their dissociation to yield –OH moieties bound to unsaturated Ti cations. Both processes contribute to induce a transition of the inherent wettability of TiO_2 surface towards a more hydrophilic state [14,37,45,46]. The acquired surface hydrophilicity may subsequently be reduced to a variable extent upon prolonged (on the timescale of a few hours) storage in air in the dark due to the restoring action of atmospheric dioxygen [14,37,45,46]. Since our UV treatments were performed at a modest illumination power (the impinging energy density was ~5 mW/cm^2), thermal degradation of the OLAC organic was unlikely to occur, so the UV treatment of the TiO_2 films was expected to drive the removal of adsorbed capping ligands and hydrophilization of the NR surfaces using the photocatalytic mechanism only.

The compositional and morphological features of the UV-irradiated thin films were investigated using EDS (Figure 5) and SEM (Figures 6–9) analyses, respectively. The collected data demonstrated that the combination of high fluence and long-lasting UV treatment is an efficient strategy to deposit uniform and compact films with low organic residue. Notably, increased compactness of TiO_2 nanostructured films is desirable in many energy-related applications because of the involved improved electron transport properties.

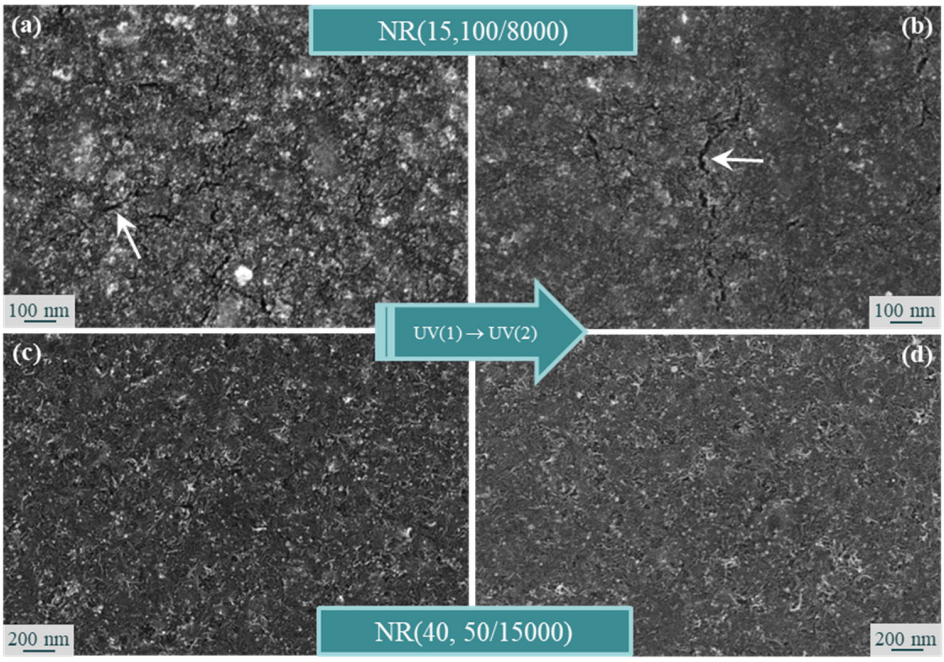

Figure 6. SEM images of NR (15, 100/8000) and NR (40, 50/15,000) subjected to the (**a**,**c**) UV(1) treatment and (**b**,**d**) UV(2) treatment, respectively. The white arrows point out the presence of cracks.

The comparison between the samples subjected to the UV(1) and UV(2) treatments evidenced that, from a morphological point of view, the samples were similar. As an example, in Figure 6, the SEM images of NR (15, 100/8000) and NR (40, 50/15,000), after the UV(1) treatment (left column) and UV(2) irradiation (right column), were compared. The overall morphologies were weakly dependent on the duration of the treatment; never-

theless, longer irradiation appeared to remove the organics more efficiently, as preliminary suggested by the higher density of areas with a "brighter" image contrast observed for the UV(1)-treated samples, corresponding to regions with a higher organic concentration.

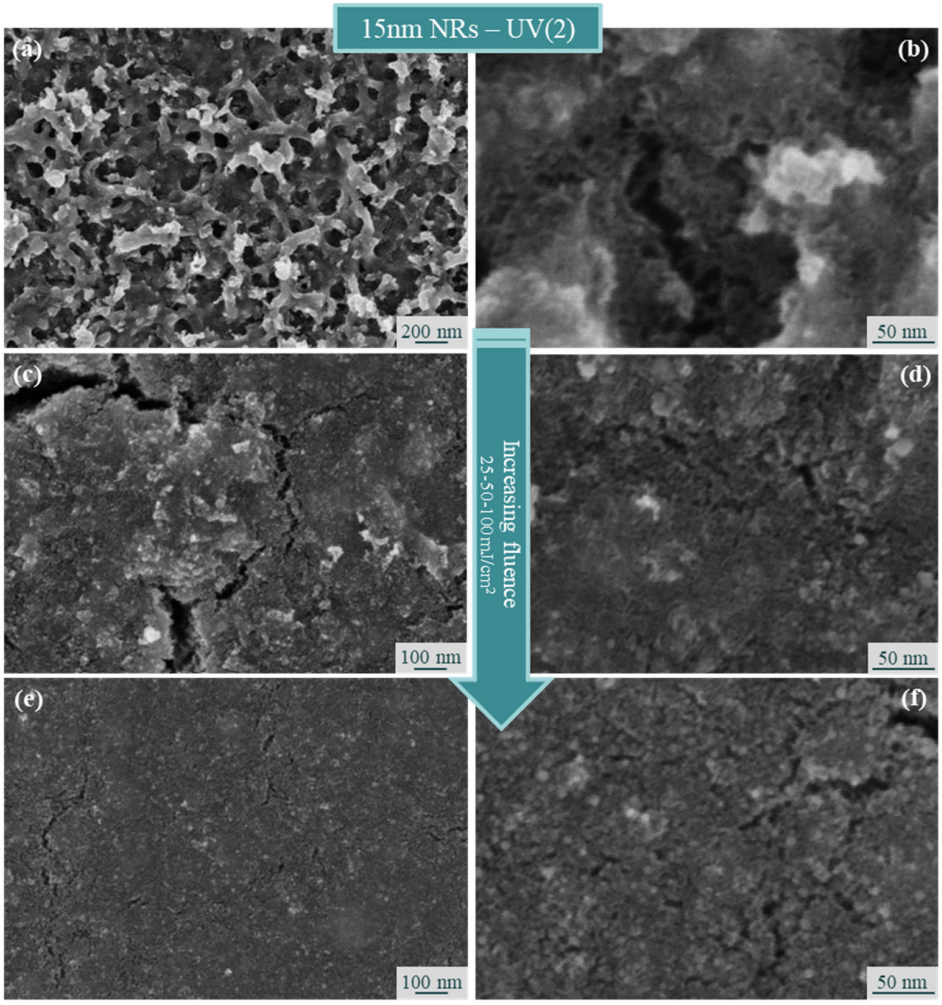

Figure 7. Low- (**left** column) and high-magnification (**right** column) SEM images of samples (**a**,**b**) NR (15, 25/20,000), (**c**,**d**) NR (15, 50/15,000) and (**e**,**f**) NR (15, 100/8000) after the UV(2) treatment.

Thus, hereafter only the samples subjected to the UV(2) treatment, that is, 14 h of irradiation, will be reported and discussed. As a result of the UV treatment, the presence of cracks, affecting mainly sample NR (15, 100/8000), after each UV treatment, was evident (see arrows in Figure 6).

Figure 7 shows the results of SEM analysis performed at different magnifications on thin films consisting of 15 nm long NRs after exposure to the UV(2) treatment. The SEM micrographs in Figure 7a,b evidence high roughness related to the high organic content of sample NR (15, 25/20,000), indicating that the UV treatment had not been effective in this case. At low magnification, a branch-like morphology similar to the one of the pristine film was evident. On the other hand, at high magnification, as a result of the longest UV treatment, which had led to removal of the organic material, the morphology of individual NRs could be discerned. Figure 7c–f report low- and high-magnification SEM images of samples NR (15, 50/15,000) and NR (15, 100/8000) after the UV(2) treatment. In comparison with the corresponding pristine samples (see Figure 3), individual NRs could still be occasionally discriminated, suggesting the effective removal of excess OLAC organic material. The presence of cracks and voids was evident as a result of the morphological changes induced by the degradation of the organic capping ligand component [50].

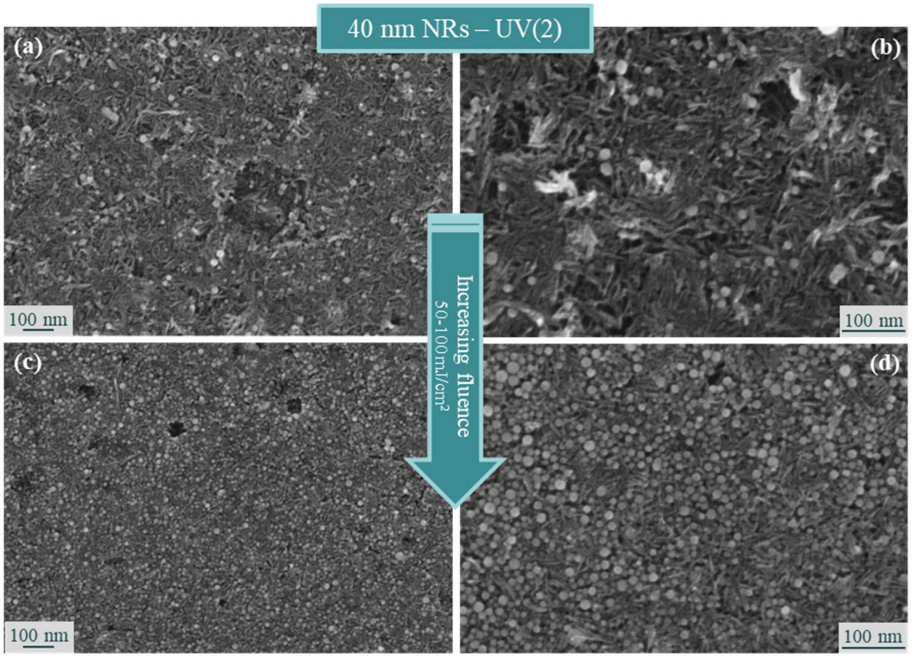

Figure 8. Low- (**left** column) and high-magnification (**right** column) SEM images of samples (**a**,**b**) NR (40, 50/15,000) and (**c**,**d**) NR (40, 100/8000) after the UV(2) treatment.

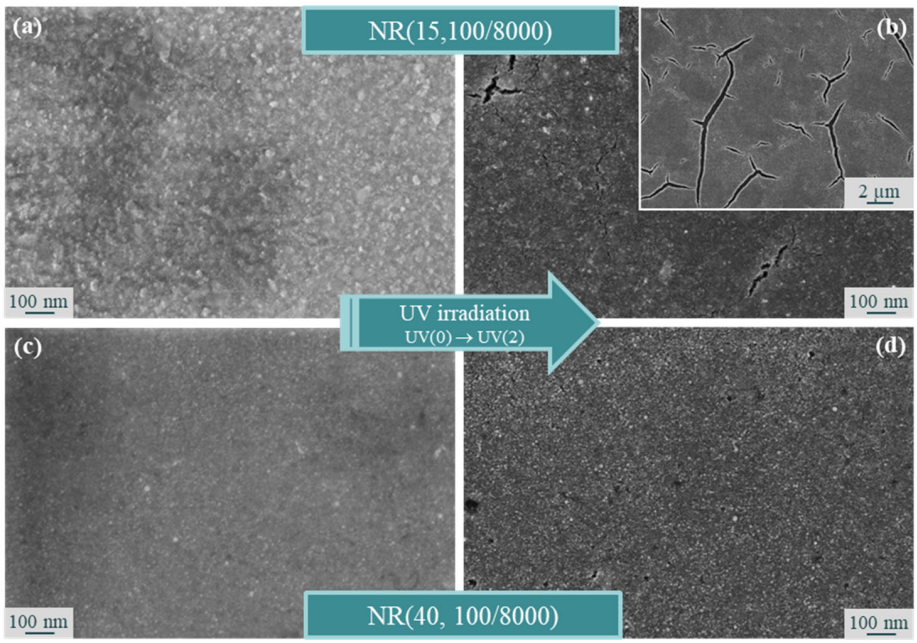

Figure 9. Comparison between the SEM images of the samples before and after the UV (2) treatment. In detail, the as-deposited samples are reported in panels (**a**) NR (15, 100/8000) and (**c**) NR (40, 100/8000). The associated UV (2) treated samples are reported in panels (**b**), and (**d**), respectively.

It is also worth noting that the laser-driven ejection conditions contributed to the removal of the organic material and to an extent were more effective for increasing the amount of energy impinging on the MAPLE target: the SEM image of the film deposited at 100 mJ/cm^2 exhibited less accentuated bright contrast features, indicating a relatively lower content of organic components.

The effect of laser fluence and UV irradiation can be definitively inferred by analyzing the variable-magnification SEM images in Figure 8, which show the morphology of samples NR (40, 50/15,000) and NR (40, 100/8000) after the UV(2) irradiation. Due to their larger

sizes, the NRs composing such thin films were more clearly identifiable in those cases, allowing a more definitive assessment of the effect of the applied UV treatment. In particular, by analyzing the morphology after the UV treatment, it was possible to better understand the effect of the laser fluence. It emerged that films prepared under different laser fluence conditions exhibited dissimilar susceptibility to undergo morphological changes under UV irradiation.

The film deposited at a laser fluence of 50 mJ/cm^2 and subjected to the UV treatment consisted of a relatively dense and uniform coverage of closely packed NRs, with an orientation parallel to the substrate; some voids could be noted, likely resulting from the rearrangement resulting from the removal of the organic material during UV irradiation. The nanorods had dimensions compatible with the ones of the pristine material. Occasionally, spherical nanoparticles with a diameter ranging from a few nanometers to approximately 20–30 nm could also be observed. On the other hand, the film deposited at a higher laser fluence of 100 mJ/cm^2 encompassed a mixture of spherical nanoparticles and pristine NRs, with a negligible density of voids. It is interesting to note that the nanorods, which were clearly distinguishable, were almost invisible in the image of the sample before the treatment (Figure 5c,d) due to the high presence of organic material embedding the NRs. Therefore, the films deposited at a higher fluence appear to have undergone a more significant modification in morphology upon UV irradiation, when compared to samples deposited at a low laser fluence.

The results discussed above demonstrate that, depending on the size of the NRs used to deposit the MAPLE films, the post-deposition UV treatment produced different outcomes. In particular, in the case of films formed of 15 nm long NRs, the formation of cracks and voids was induced, which was almost negligible in the case of films formed of 40 nm long NRs. This was demonstrated in Figure 9, which compared the morphologies of samples NR (15, 100/8000) and NR (40, 100/8000) before and after UV(2) irradiation.

Before irradiation (label UV(0)), both samples exhibited an image contrast degraded by charging effects due to the insulating nature of the capping ligands on the TiO_2 surface, making the fine details of the morphology hardly observable. After irradiation (label UV(2)), both samples exhibited a more homogeneous contrast, typical of a conductive material. The sample NR (15, 100/8000), which was treated with UV(2) (Figure 9b, and its inset), showed the formation of cracks, which likely resulted from the removal of a higher quantity of organic material with respect to the film consisting of 40 nm long NRs. This was confirmed with the EDS analyses, which demonstrated a much higher reduction of C content in the case of the films embedding 15 nm NRs than for the films consisting of 40 nm long ones. As a matter of fact, the Ti/C ratio increased by a factor of 5 (at 50 mJ/cm^2) to 7 (at 100 mJ/cm^2) for the sample with 15 nm NRs and by a factor of 3.2 (at 50 mJ/cm^2) to 5 (at 100 mJ/cm^2) for the sample with 40 nm NRs. All of this clearly demonstrates that the C content in the as-deposited samples composed of the smallest NRs was higher; therefore, the removal of organic material using UV irradiation can concur with the formation of cracks.

Figure 4c–f report the results of the EDS-based elemental analysis carried out after UV(2) treatment, compared with the results obtained from the pristine samples. All samples featured a reverse of the Ti/C versus Ti/O ratios, with the former being higher than the latter in the UV-treated samples with respect to the as-deposited sample. The strong increase of the Ti/C ratio after UV exposure demonstrated the effective removal of a significant fraction of OLAC- and OLAM-capping molecules. On the other hand, the far less pronounced dependence of the Ti/O ratio (recall that the content of O is mostly dictated by the amount of O in the TiO_2 lattice of the NRs) on the UV irradiation was due to the modest relative fraction of O associated with the OLAC ligands that were eliminated, which was partly compensated for using photo-induced surface hydroxylation of the TiO_2 surfaces [14,37,45,46]. Surface hydroxylation may also explain the increasing intensity of O contribution after the UV treatment (despite OLAC ligands being expected to be degraded), which was in agreement with previous investigations [37,46].

The lower magnification SEM images also disclosed some interesting and unexpected evidence of our experiments, revealing the absence of the distinctive surface morphologies/patterns of MAPLE deposits [40,51]. Unequivocal confirmation of this issue was provided in Figure 10, which reports a (30 × 20) μm^2 large area of sample NR (15, 25/20,000) (Figure 10a) and a (8 × 5) μm^2 area of sample NR (15, 50/15,000) (Figure 10b). It was evident that there was an absence of micrometer-sized solvent evaporation patterns or deflated balloons or globules, even for the lowest fluence value (25 mJ/cm^2), which instead would be expected to favor a higher amount of residual solvent reaching the substrate. This peculiar issue in our experiments is particularly interesting due to the implications for the achievement of MAPLE films with improved surface quality and will be discussed hereafter in a dedicated section.

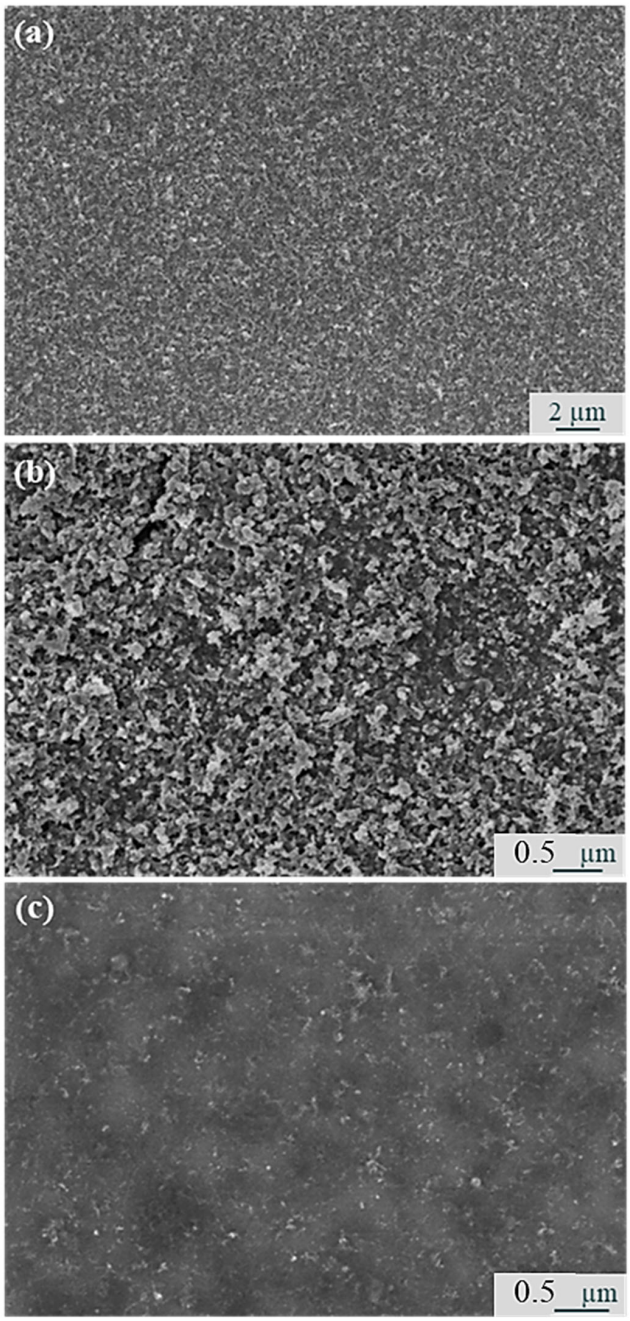

Figure 10. SEM plan-view images of samples (**a**) NR (15, 25/20,000), (**b**) NR (15, 50/15,000) and (**c**) NR (40, 50/15,000), demonstrating the absence of the distinctive micrometer-sized patterns of the MAPLE deposits on a suitably large scale.

3.4. Contact Angle Measurements

The monolayer of OLAC and OLAM molecules capping the TiO_2 NRs renders them hydrophobic and highly dispersible in non-polar solvents. As a typical photosensitive functional material, the wettability of TiO_2 can be reversibly switched between hydrophobic and hydrophilic under UV light [14,37,45,46]. As recalled earlier, UV irradiation of TiO_2 underlies two concomitant surface-confined mechanisms, namely, partial or total photocatalytic removal of any adsorbed alkyl compounds (e.g., atmospheric hydrocarbon contaminants and/or organic capping ligands, as in the present case) and photoinduced surface hydroxylation upon dissociative/non-dissociative adsorption of atmospheric H_2O [14,37,45,46]. Depending on their actual relevance, these processes may macroscopically reflect into a wettability transition of theTiO_2 surface from an initial hydrophobic state to a more hydrophilic one [14,37,45,46]. Following the UV treatment, –OH groups that may be adsorbed onto the NR surface indicate the onset of the transition from an hydrophobic surface to an hydrated surface through the removal of surfactants [37,46].

Water contact angle (WCA) measurements were therefore performed on the UV-irradiated TiO_2 NR-based thin films to study their susceptibility to photocatalytically induced surface hydrophilicization [45]. In the case of TiO_2 NRs exposing the alkyl chains of the surface-bound oleate ligands, the photo-oxidation mainly caused the degradation of the organic capping layer, thus leaving a hydrophilic TiO_2 surface.

Representative results of the impact on WCA of the UV exposure of the films under study are illustrated in Figure 11 and summarized in Table 1. Following the UV(1)-treatment, WCA values of all the TiO_2 NR films decreased significantly (Table 1 and Figure 11), thus confirming the UV-driven change of the surface wettability towards a more hydrophilic state (note that the inherent film roughness also contributes to determine the ultimate film wettability [37,46].

Interestingly, the as-deposited NR films consisting of 15 nm long NRs initially showed an increasingly hydrophilic surface at increasing fluences of deposition, meaning that the removal of surface-bound surfactants may occur to an appreciable extent already during film deposition. A similar effect was not observable for the as-deposited films embedding the 40 nm long NRs, which appeared to be more hydrophilic, regardless of the fluence set. Such different behavior may be explained by the more compact and regular self-assembly of the nanostructures within the films (see SEM images), which reduced the surface roughness and hence the resulting wettability. The EDS measured change in the Ti/C signal ratio (Figure 5) confirmed that the organic-capping molecules, which were removed only partially from 15 nm long NR films when deposited at higher fluences, could be massively removed after UV-treatment.

3.5. Spectral Characterization

Figure 12 shows the UV-Vis transmittance spectra (Figure 12a,b) and the absorbance curves (Figure 12c,d) of the samples consisting of 15 nm and 40 nm long TiO_2 NRs deposited at different laser fluence values and compares them with the spectrum of the same sample following UV treatment. It was evident that the major differences occurred in the case of the shortest TiO_2 NRs and the highest fluence. For the 40 nm long NRs, the removal of the OLAC and OLAM capping using the UV treatment resulted in slightly increased transparency at any deposition fluence; such an effect could not be systematically observed for the 15 nm long NRs. Indeed, samples NR (15, 50/15,000) and NR (15, 100/8000) exhibited reduced rather than increased mean transmittance following the UV treatment. Since the presence of OLAM or OLAC has no substantial impact on the absorption properties of colloidal nanocrystals [52], the above experimental findings can be explained on the basis of the changes in morphology and microstructure (mean volume density, mode of NR packing, etc.) of the 15 nm NR-based thin films observed for increasing fluence and following UV irradiation. The fundamental exciton absorption of TiO_2 accounted for the reduction in transmittance and enhancement of absorbance below 400 nm.

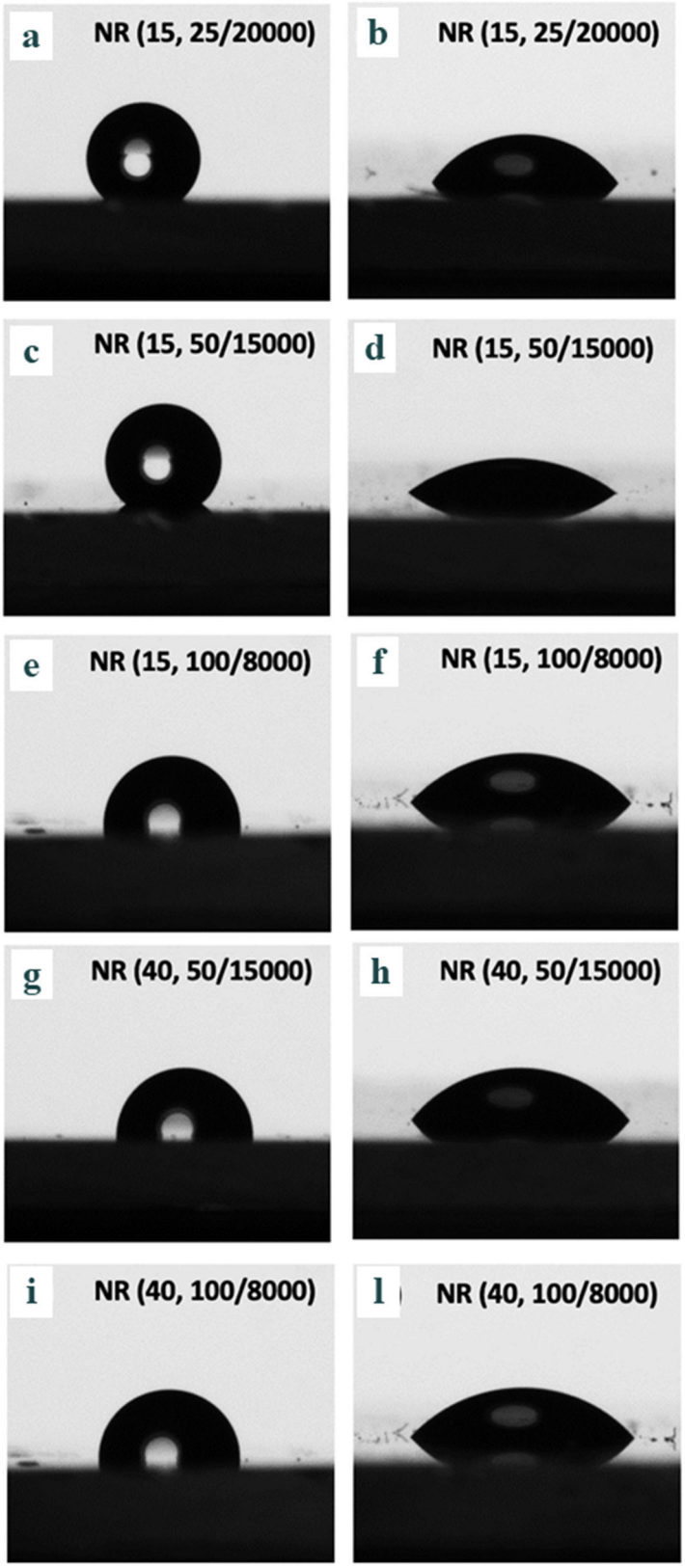

Figure 11. Photographs showing the WCA measured before (**left** column) and after (**right** column) the UV(1) treatment of the samples under consideration in this study and named according to the nomenclature detailed in Table 1.

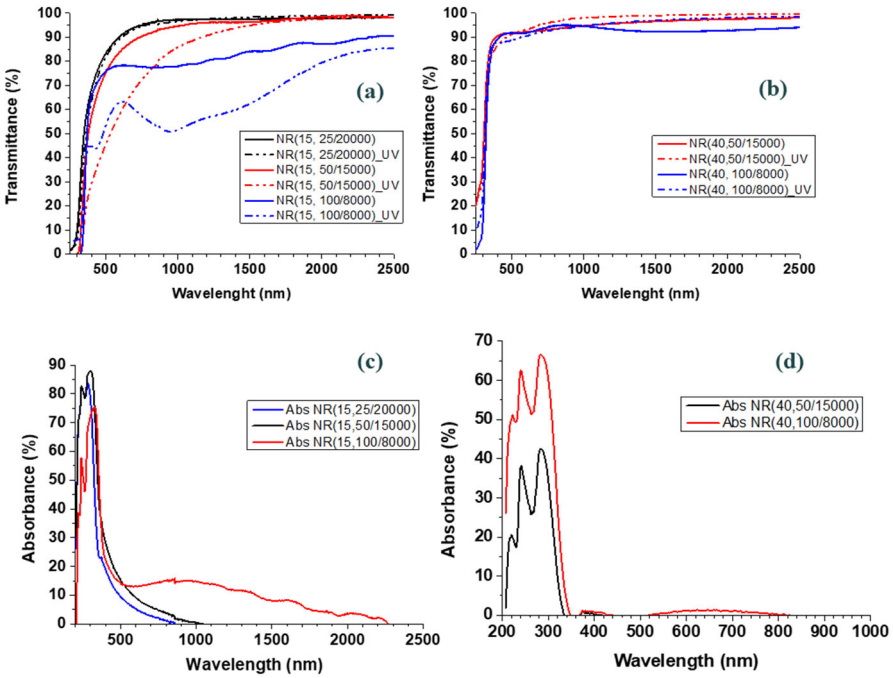

Figure 12. UV-Vis (**a**,**b**) transmittance spectra and (**c**,**d**) absorbance curves of the thin films consisting of 15 nm and 40 nm long TiO_2 NRs deposited at different laser fluence values (F = 25, 50, 100 mJ/cm^2) before and after the UV-treatment.

4. Discussion

Thin films of colloidal anatase-phase TiO_2 NRs deposited using the MAPLE technique are discussed with regard to two main aspects. First, the impact of the capping surfactants bound to the surface of the nanorod precursors on film morphology, compactness and uniformity. Second, the influence of laser fluence and post-growth UV-light exposure on possible thermally induced and photochemical pathways of degradation/removal of the organic coating molecules.

The main pieces of evidence that can be drawn from the analysis of our MAPLE-deposited thin films made of colloidal TiO_2 NRs are the following: (i) depositions carried out at relatively higher laser fluences led to films characterized by an overall reduced mass fraction of the organic component, associated with the surfactant derivatives that passivate the surface of the individual TiO_2 NR precursors; (ii) after deposition, the remaining capping molecules on the as-synthesized TiO_2 NRs may have been photocatalytically removed from the as-prepared films upon prolonged band-gap excitation with UV light under ambient conditions; and (iii) the as-deposited films did not exhibit the micrometer-sized surface features (commonly, ring-like evaporative patterns, globules and deflated balloons) that typically affect MAPLE deposits [51]. In particular, the latter outcome was an unexpected experimental finding that deserves to be rationalized owing to its fundamental and practical implications for the growth of functional thin films using MAPLE. On the basis of the overviewed experimental evidence two main aspects are remarkable that will be discussed in the following subsections.

4.1. Impact of Laser Fluence and Post-Growth UV Treatment on the Stability of the Capping Ligands

The MAPLE technique works in such a way that the solvent screens the solute substantially from the UV laser irradiation. However, laser absorption from the solute may still occur to an appreciable extent, depending on the concentration and absorption properties of the solute. As a consequence of laser-induced heating, fluence-dependent rod-to-sphere

shape transformation was reported following the deposition using the MAPLE technique of colloidal TiO_2 NR precursors [35]. Hence, other important factors to take into account are the thermal stability behavior of the OLAC/OLAM-capping molecules under laser irradiation and the effect of the warming-up of the MAPLE target in reducing/removing the organic capping.

Under our experimental conditions, all components of the MAPLE target (toluene, capping ligands on the TiO_2 NRs and anatase phase TiO_2 lattice) absorbed at the 248 nm excitation laser wavelength. In particular, it should be considered that the OLAC/OLAM molecules start to absorb at wavelengths below 320 nm [37]; therefore, their absorption at the 248 nm laser wavelength implies that laser-driven photo-dissociation/degradation cannot be ruled out.

A literature survey indicated that the annealing of anatase TiO_2 NRs at temperatures of up to 150 °C is unable to remove the organic shell of surface-bound surfactants [38] and thermal degradation of the surfactants may take place at temperatures greater than 150 °C under an inert N_2 atmosphere [53,54]. Under such conditions, endothermic reactions observed at 105 °C, 265 °C and 436 °C were ascribed, respectively, to solvent removal, detachment of the surfactant molecules from the TiO_2 lattice and fragmentation of their alkyl chains, and finally, the complete degradation of the resulting organic subunits. Other experiments pointed out that the thermal decomposition of capping surfactants is environment-dependent and can occur at higher temperatures and in successive steps through channeling of the adsorbed heat into fragmentation of the alkyl backbone. The most relevant mass losses during thermal degradation of surfactant-capped anatase TiO_2 NRs are associated with the removal of physisorbed water at 50–150 °C and with the progressive decomposition of the surface-bound surfactants at temperatures between 200 and 500 °C [38].

As the temperature of the MAPLE target was expected to be higher than 150 °C [35], increasing fluence beyond a critical threshold may be responsible for thermally driven degradation of the organic molecules capping the NRs. However, our experimental evidence indicated that, within the range of fluence conditions applied in our MAPLE experiments, the organic capping ligands were eliminated only partially from the TiO_2 NR precursors during their deposition. This issue is also relevant in practice because the presence of surface-bound organic ligands affects the spatial organization of TiO_2 NRs by governing their mutual interactions. The critical role of the head groups and molecular structure of the capping ligands in the self-assembly of colloidal nanoparticles into mesoscopic superstructures with variable degree of ordering is well documented in the literature [55,56]. Definitively, the results reported in this study highlighted the role played by the organic-capping molecules on the surface of nanostructures in terms of the final morphology and arrangement of nanostructured films deposited using the MAPLE technique.

4.2. Absence of the Characteristic Surface Morphologies Produced by the Deposition Mechanisms Underlying the MAPLE Technique

An interesting piece of evidence from our experiments was the absence of the characteristic surface morphological features of MAPLE-deposited films [51], including collapsed pipes, large aggregates, deflated balloons, sparsely overlapping bubble-like structures and hollow ring-like evaporative traces with sizes spanning from tens of nanometers to tens of microns. Such an outcome cannot be ascribed to the post-growth UV treatment because the distinctive features mentioned above were not observed in any of the as-deposited films, including those prepared at the lowest fluence value (Figure 10) for which residual solvent reaching the substrate might be expected.

In general, it should be recalled that MAPLE is a pseudo-dry technique. This aspect impacts the morphology of the deposit, leading to the occurrence of complex surface features, including patterns related to the evaporation of the residual solvent, which lead to rough films with roughness increasing for increasing laser fluence [39,40,49,57–59].

These surface features were theoretically explained by invoking the establishment of a laser-target explosive-interaction regime above a threshold fluence, where the overheated matrix abruptly ejects solvent droplets and solute–solvent bubbles with characteristic sizes ranging from tens of nanometers to tens of microns [40]. Such ejected objects evolve in shape and size during their landing towards the substrate. Unlike in the idealized picture of MAPLE as a solvent-free technique, solvent liquid droplets and solute–solvent bubbles arrive onto the substrate and collapse into complex surface morphologies and surface hollow rings following evaporation of the residual solvent [51]. Since these mechanisms are intrinsically related to the mechanisms underlying the MAPLE processes, the occurrence of surface features degrading the deposit quality would be expected to be unavoidable.

In order to explain our unconventional experimental findings, we tentatively propose a picture based on the behavior of a model system consisting of a liquid droplet embedding non-volatile species (that is, toluene droplets including surfactant-capped TiO_2 NRs in our specific case), which impacts onto a textured substrate with texture owed to the roughness produced by an irregular distribution of the previously deposited OLAC-capped TiO_2 NRs.

In general, droplets containing a relatively low volatility substance always form complex patterns following evaporation [50,60–63]. In particular, a liquid droplet hitting a dry substrate tends to spread laterally and its side lamella may (i) deposit on the surface while keeping the integrity of the drop, (ii) splash (yielding prompt splashing or corona splashing) or (iii) bounce off the surface depending on the deposition kinematics, the physical properties of the droplet liquid, the substrate and the surroundings. The roughness of the substrate and slope of the substrate corrugations (as in the case of micro-structured surfaces) play an important role in determining the evaporation rate (that is higher on rough substrates than on the smooth substrates due to reduced wetting surface), the formation of given patterns by drying droplets [64] and the transition from spreading to splashing [65–67]. In particular, roughness and textured surfaces can strongly decrease or suppress splashing effects [65,66], and the height of the surface features plays a decisive role in determining the reduction/suppression of splashing [65].

Under our experimental conditions, the wetting, porosity and roughness properties of the films made of TiO_2 NRs depended on the amount of the associated OLAC/OLAM surfactants. Due to the high roughness, which was pointed out with the SEM analysis, and energetics involved in the MAPLE mechanisms, solute–toluene bubbles and pure solvent drops should promptly splash rather than spreading onto the substrate. Indeed, in general, circular evaporation rings may form, depending on the competition between the solvent evaporation rate and diffusion rate of the deposited species. However, "fracturing" of the volatile toluene droplets hitting the substrate does not favor the formation of ring-like evaporative patterns and speeds up the evaporation of the residual solvent. On the other hand, channeling of the deposited solvent through voids and surface-exposed TiO_2 NRs during growth is highly likely to occur. As a consequence, the evaporation dynamics on a free and flat surface are likely to be less relevant, and hence are not able to explain the final film morphology. The above argument was strongly suggested by the relationships between the observed morphology changes and the removal of organics driven by the UV treatment, which has been discussed earlier.

On the other hand, the formation of solute–solvent droplets and the solvent–solute interaction within the plasma plume were expected to be affected by the occurrence of the organic capping due to its impact on the solubility of the TiO_2 NRs and the interaction of the latter with the environment. In particular, as the organics capping TiO_2 NRs inhibit aggregation effects, the confinement of capped TiO_2 NRs within the plasma plume in the presence of toluene droplets is unlikely to favor the formation of large solute–solvent clusters embedding a larger fraction of solvent.

Therefore, in our experimental conditions, the absence of the characteristic surface morphological features of MAPLE-deposited films may have resulted from the interplay between the impact of the organic capping on the formation and evolution of the solvent–solute cluster within the expanding plasma plume and the roughness, wettability and porosity characteristics of the surfaces of the growing films.

4.3. Shape and Phase Stability in Maple Experiments

The SEM investigation of the MAPLE-deposited TiO_2 NR films under study demonstrated the occurrence of rod-to-sphere shape changes depending on the fluence values caused by the laser induced heating. It is interesting to discuss this occurrence in terms of laser-induced phase-changes to assess the practical implications of this phenomenon.

As outlined in the introduction, TiO_2 is a polymorphic material that can crystallize in different phases, among which there are anatase, rutile and brookite phases. While rutile is the most thermodynamically stable phase in the temperature range 600–1855 °C, the formation of the metastable anatase is kinetically preferred (sometimes leading to co-existence of brookite) under ordinary synthesis conditions at temperatures below ~400 °C. Once formed, pure anatase TiO_2 can remain stable at temperatures as high as 800–900 °C [68]. The irreversible anatase-to-rutile phase transition can generally be initiated at temperatures of approximately 600 °C, beyond which rutile becomes increasingly favored upon prolonged heat treatment [69].

The anatase-to-rutile transformation is affected by several physical and chemical factors, including the size/shape (hence, the surface area) and degree of lattice crystallinity (affected by defects, such oxygen vacancies, interstitials, dopants, etc.) of the domains that compose the solid, the structure and extension of grain boundaries (in polycrystalline solids), the type of atmosphere and heating mode and rate. These parameters come into play in the possible mechanisms of phase transformation [69–74].

In particular, oxygen vacancies are known to decisively accelerate the kinetics of the phase transformation by enhancing lattice relaxation and favoring ion rearrangement. However, in our experiments, MAPLE deposition of the colloidal TiO_2 NRs was accomplished under vacuum, that is, in neither a reducing nor oxidizing atmosphere that could otherwise have contributed to modify the concentration of the oxygen vacancies in the NR lattice.

On the other hand, laser-induced heating could play a role in driving a phase transition of the precursor TiO_2 NRs. To date, MAPLE experiments using a KrF excimer laser (λ = 248 nm, τ = 20 ns) have indicated that brookite-phased TiO_2 NRs initially dissolved in toluene can undergo a transition to rutile, accompanied by a rod-to-sphere shape change if deposited at a fluence as high as F = 350 mJ/cm^2 [35,48]. Such a phase transformation was found to be inhibited by alleviating the impact of laser-driven heating if the MAPLE process is carried out at a reduced laser fluence [35,48]. As at the nanoscale the activation energies for anatase-to-brookite and anatase-to-rutile transitions are in the same order of magnitude as that of the brookite-to-rutile, then the starting anatase TiO_2 NRs can be expected to escape laser-induced conversion to other phases if deposited from toluene solutions at a sufficiently low fluence. In line with these findings, it has been shown that anatase TiO_2 nanoparticles deposited from a suspension in deionized water using ArF excimer laser (λ = 193 nm, τ = 20 ns) at a high fluence of F = 550 mJ/cm^2 retained their pristine crystal phase [47]. In addition, it has been found that the phase transformation of anatase nanoparticles with an elongated shape to rutile requires an activation energy much higher than that for spherical nanoparticles, which implies that the former exhibit higher thermal stability than the latter [71]. Theoretical calculations of the physical-chemical properties of TiO_2 nanostructures have predicted a similar shape dependence of the melting temperature for different TiO_2 polymorphs [75].

The anatase-to-rutile transition induced using laser irradiation in an oxygen environment of TiO_2 nanoparticles requires extended periods of high-intensity continuous-

laser irradiation (up to 5 h) to promote heating of the surface and the formation of high-temperature plasma to drive oxygen dissociation and its reaction with titanium [72]. Unlike direct laser irradiation of TiO_2, during the MAPLE the target of our experiments, TiO_2 NRs, were shielded by the highly absorbing solvent, toluene. Hence, the temperature evolution and heating of the target were mainly due to the solvent absorption efficiency and fluence value. In particular, as toluene exhibits high absorption at the operating wavelength of our experiments, fluence is the key parameter to be tuned in order to change the heat transfer of the laser pulses to the TiO_2 NRs.

To summarize, the effective control of rod-to-sphere shape transition and/or anatase-to-rutile phase conversion is possible with a proper calibration of the fluence conditions, meaning that mild fluence conditions rule out any shape and phase change. This outcome implies that the MAPLE technique can be exploited to deposit titania nanorod films by retaining the shape and phase of the precursor nanoparticles in addition to offering the advantages of the technique outlined in the introduction. Post-growth degradation and removal of the organic materials can be effectively achieved using an UV treatment.

As a final remark, the possible occurrence of a partial anatase-to-rutile phase change would not necessarily be undesirable. For example, the photocatalytic performance of the films could be enhanced if they embedded a suitable spatial distribution of anatase–rutile heterojunction, at which exciton dissociation could be promoted [76].

5. Conclusions

In this paper, MAPLE deposition and characterization of TiO_2 NRs have been carried out systematically. The role of the organic capping covering the surface of the nanorods and its impact on the morphology, composition, wettability and optical properties of the deposited thin films has been studied as a function of the deposition conditions (in particular laser fluence), post-deposition treatments (UV irradiation) and length of the nanorods. Indirect evidence of the presence of organic material in the deposited films has been provided using SEM and EDS investigations by monitoring in parallel any changes in the C signal, which is related to the organic material, and the contrast in SEM images. Indeed, since samples embedding organic material are non-conductive, charging effects occurring during the electron beam scanning imply that the brighter the contrast appears, the greater the organic content is. Moreover, an increased visibility of the nanostructures under an electron beam is indicative of a decreased amount of the organic material. This methodological approach has been applied to demonstrate the concurrent effect of laser fluence and UV irradiation in the removal of the organic capping.

In particular, while the reduction of organic materials caused by increasing laser fluence has been demonstrated using EDS chemical investigations, the enhanced visibility of the nanorod morphology after UV irradiation (as revealed using SEM analyses) demonstrated the stronger effectiveness of a UV irradiation protocol in the removal of the organic matrix embedding the NRs.

The wettability investigation confirmed the EDS data by demonstrating an increased hydrophilicity of all the MAPLE films after UV treatment. The higher water wettability after UV treatment was expected because photo-oxidation leads to the exposure of the hydroxyl group of TiO_2 NRs and hydration of the substrate.

The collected data demonstrated that the combination of high fluence and long-lasting UV treatment is an efficient strategy to deposit uniform and compact films with low organic residuals. In particular, changes in the porosity/compactness/uniformity of TiO_2 nanostructured films and their purity are relevant for practical applications because of the impact on the surface area and density of active sites, and, as a consequence, on the intensity and effectiveness of the signal related to the photogenerated and collected charges. Electron transport may be a limiting factor for less compact films without percolated patterns allowing charge carrier mobility and transfer. Therefore, high compactness improves

electron transport, leading to a higher conversion efficiency and photoelectrochemical performance. On the other hand, the presence of surface organic agents can alter the thermodynamic stability, optical properties, photocatalytic activity, chemical reactivity and antibacterial activity.

Seemingly, an apparently marginal, but extremely important result of our experiments, was the absence from all the investigated samples of the characteristic (undesired) patterns and surface features which are well known to be unavoidable and typically degrade the morphological quality of the films prepared using the MAPLE technique. Even though this result was achieved serendipitously, it was worth being reported because of its consequence from both the fundamental and practical viewpoints. Indeed, our results have demonstrated that, although post-deposition UV treatment is needed to obtain degradation/removal of the organic capping, the occurrence of organics is beneficial to modify the deposition and drying dynamics of the residual solvent, which was toluene in our experiments. Hence, while mild fluence conditions which retain the shape and phase of the precursor titania nanoparticles would be unfavorable for effective solvent removal, on the other hand they are beneficial because of the ineffective removal of the organic capping material.

A tentative explanation for the absence of the characteristic MAPLE patterns in the specific case of our materials has been proposed based on the splashing dynamics of solvent droplets on rough surfaces and on the implications of the organic capping for the formation and evolution of solute–solvent clusters within the plasma plume. Our findings are likely to stimulate further focused investigations on organic capping-free nanostructured films deposited using MAPLE with the aim of overcoming some of the main defects in the quality features of thin films achievable with this technique and of understanding their origin at the microscopic level.

As a final remark, the presence of toluene photolysis-induced particulates was observed under multi-pulse laser irradiation of frozen targets consisting of multi-wall carbon nanotubes dispersed in toluene under background pressures from 10^{-2} to 10^{-3} Pa [77,78]. The amount of such particulates was found to increase for fluence values surpassing the 200 J/cm^2 threshold value. In MAPLE experiments, the highly vaporized residual solvent reaching the substrate can be minimized using several experimental tricks, for instance, using high vacuum background pressure, a large enough target-to-substrate distance and an efficient evacuation pumping system of the deposition chamber. All of this was accomplished in our MAPLE experiments. Notably, the fluence values set in our experiments were much lower than even the threshold fluence yielding a relevant generation of toluene-related particulates reported in the literature [77,78].

On the other hand, the degradation and removal of toluene vapor is highly likely to occur under our experimental conditions: the use of short-wavelength UV (254 + 185 nm) irradiation in the presence of TiO_2 catalyst was observed to favor photodegradation of gaseous toluene because of the combined effect of photochemical oxidation in the gas phase and photocatalytic oxidation on TiO_2 [79].

Further experiments, that are out of the focus of the present study may address the eventual generation of toluene solvent-related byproducts that would be degraded by the UV-driven post-growth treatment needed to remove the organic capping encasing the TiO_2 NRs.

Author Contributions: Conceptualization, formal analysis, MAPLE experiments, data curation, writing—original draft preparation, writing—review and editing, supervision, M.C.; SEM and EDS analyses, writing—original draft preparation, writing—review and editing, A.T.; synthesis of the TiO_2 precursor solutions; UV-treatments, writing, review and editing, P.D.C.; wettability measurements, writing, review and editing V.A.; MAPLE experiments, data curation, writing—review and editing, supervision, A.P.C. All authors have read and agreed to the published version of the manuscript.

Funding: This research received no external funding.

Data Availability Statement: Data may be made available on request.

Acknowledgments: The authors acknowledge Sonia Carallo for UV treatments and Corrado Massimo for their technical assistance during the MAPLE depositions.

Conflicts of Interest: The authors declare no conflict of interest.

References

1. Sagadevan, S.; Imteyaz, S.; Murugan, B.; Lett, J.A.; Sridewi, N.; Weldegebrieal, G.K.; Fatimah, I.; Oh, W.-C. A Comprehensive Review on Green Synthesis of Titanium Dioxide Nanoparticles and Their Diverse Biomedical Applications. *Green Process. Synth.* **2022**, *11*, 44–63. [CrossRef]
2. Winkler, H.C.; Notter, T.; Meyer, U.; Naegeli, H. Critical Review of the Safety Assessment of Titanium Dioxide Additives in Food. *J. Nanobiotechnol.* **2018**, *16*, 51. [CrossRef] [PubMed]
3. Carp, O.; Huisman, C.L.; Reller, A. Photoinduced Reactivity of Titanium Dioxide. *Prog. Solid State Chem.* **2004**, *32*, 33–177. [CrossRef]
4. Kumar, A.; Choudhary, P.; Kumar, A.; Camargo, P.H.C.; Krishnan, V. Recent Advances in Plasmonic Photocatalysis Based on TiO_2 and Noble Metal Nanoparticles for Energy Conversion, Environmental Remediation, and Organic Synthesis. *Small* **2022**, *18*, 2101638. [CrossRef] [PubMed]
5. Haider, A.J.; Jameel, Z.N.; Al-Hussaini, I.H.M. Review on: Titanium Dioxide Applications. *Energy Procedia* **2019**, *157*, 17–29. [CrossRef]
6. Diebold, U. Structure and Properties of TiO_2 Surfaces: A Brief Review. *Appl. Phys. A* **2003**, *76*, 681–687. [CrossRef]
7. Arun, J.; Nachiappan, S.; Rangarajan, G.; Alagappan, R.P.; Gopinath, K.P.; Lichtfouse, E. Synthesis and Application of Titanium Dioxide Photocatalysis for Energy, Decontamination and Viral Disinfection: A Review. *Environ. Chem. Lett.* **2023**, *21*, 339–362. [CrossRef]
8. Wang, J.; Wang, Z.; Wang, W.; Wang, Y.; Hu, X.; Liu, J.; Gong, X.; Miao, W.; Ding, L.; Li, X.; et al. Synthesis, Modification and Application of Titanium Dioxide Nanoparticles: A Review. *Nanoscale* **2022**, *14*, 6709–6734. [CrossRef]
9. Anucha, C.B.; Altin, I.; Bacaksiz, E.; Stathopoulos, V.N. Titanium Dioxide (TiO_2)-Based Photocatalyst Materials Activity Enhancement for Contaminants of Emerging Concern (CECs) Degradation: In the Light of Modification Strategies. *Chem. Eng. J. Adv.* **2022**, *10*, 100262. [CrossRef]
10. Fujishima, A.; Honda, K. Electrochemical Photolysis of Water at a Semiconductor Electrode. *Nature* **1972**, *238*, 37–38. [CrossRef]
11. Wang, J.; Guo, R.; Bi, Z.; Chen, X.; Hu, X.; Pan, W. A Review on TiO_{2-x}-Based Materials for Photocatalytic CO_2 Reduction. *Nanoscale* **2022**, *14*, 11512–11528. [CrossRef] [PubMed]
12. Ohtani, B. Titania Photocatalysis beyond Recombination: A Critical Review. *Catalysts* **2013**, *3*, 942–953. [CrossRef]
13. Reghunath, S.; Pinheiro, D.; KR, S.D. A Review of Hierarchical Nanostructures of TiO_2: Advances and Applications. *Appl. Surf. Sci. Adv.* **2021**, *3*, 100063. [CrossRef]
14. Fujishima, A.; Zhang, X.; Tryk, D.A. TiO_2 Photocatalysis and Related Surface Phenomena. *Surf. Sci. Rep.* **2008**, *63*, 515–582. [CrossRef]
15. Diebold, U. The Surface Science of Titanium Dioxide. *Surf. Sci. Rep.* **2003**, *48*, 53–229. [CrossRef]
16. Zhang, H.; Banfield, J.F. Structural Characteristics and Mechanical and Thermodynamic Properties of Nanocrystalline TiO_2. *Chem. Rev.* **2014**, *114*, 9613–9644. [CrossRef]
17. Caricato, A.P.; Arima, V.; Catalano, M.; Cesaria, M.; Cozzoli, P.D.; Martino, M.; Taurino, A.; Rella, R.; Scarfiello, R.; Tunno, T.; et al. MAPLE Deposition of Nanomaterials. *Appl. Surf. Sci.* **2014**, *302*, 92–98. [CrossRef]
18. Luttrell, T.; Halpegamage, S.; Tao, J.; Kramer, A.; Sutter, E.; Batzill, M. Why Is Anatase a Better Photocatalyst than Rutile?—Model Studies on Epitaxial TiO_2 Films. *Sci. Rep.* **2014**, *4*, 4043. [CrossRef]
19. Scanlon, D.O.; Dunnill, C.W.; Buckeridge, J.; Shevlin, S.A.; Logsdail, A.J.; Woodley, S.M.; Catlow, C.R.A.; Powell, M.J.; Palgrave, R.G.; Parkin, I.P.; et al. Band Alignment of Rutile and Anatase TiO_2. *Nat. Mater.* **2013**, *12*, 798–801. [CrossRef]
20. Duminica, F.-D.; Maury, F.; Senocq, F. Atmospheric Pressure MOCVD of TiO_2 Thin Films Using Various Reactive Gas Mixtures. *Surf. Coat. Technol.* **2004**, *188–189*, 255–259. [CrossRef]
21. Shi, J.; Wang, X. Growth of Rutile Titanium Dioxide Nanowires by Pulsed Chemical Vapor Deposition. *Cryst. Growth Des.* **2011**, *11*, 949–954. [CrossRef]
22. Nezar, S.; Saoula, N.; Sali, S.; Faiz, M.; Mekki, M.; Laoufi, N.A.; Tabet, N. Properties of TiO_2 Thin Films Deposited by Rf Reactive Magnetron Sputtering on Biased Substrates. *Appl. Surf. Sci.* **2017**, *395*, 172–179. [CrossRef]
23. Mahshid, S.; Askari, M.; Ghamsari, M.S.; Afshar, N.; Lahuti, S. Mixed-Phase TiO_2 Nanoparticles Preparation Using Sol–Gel Method. *J. Alloys Compd.* **2009**, *478*, 586–589. [CrossRef]
24. Park, H.K.; Moon, Y.T.; Kim, D.K.; Kim, C.H. Formation of Monodisperse Spherical TiO_2 Powders by Thermal Hydrolysis of $Ti(SO_4)_2$. *J. Am. Ceram. Soc.* **1996**, *79*, 2727–2732. [CrossRef]
25. Zhao, Z.; Tay, B.K.; Yu, G. Room-Temperature Deposition of Amorphous Titanium Dioxide Thin Film with High Refractive Index by a Filtered Cathodic Vacuum Arc Technique. *Appl. Opt.* **2004**, *43*, 1281–1285. [CrossRef]

26. Tang, D.; Cheng, K.; Weng, W.; Song, C.; Du, P.; Shen, G.; Han, G. TiO_2 Nanorod Films Grown on Si Wafers by a Nanodot-Assisted Hydrothermal Growth. *Thin Solid Film.* **2011**, *519*, 7644–7649. [CrossRef]
27. Kumi-Barimah, E.; Penhale-Jones, R.; Salimian, A.; Upadhyaya, H.; Hasnath, A.; Jose, G. Phase Evolution, Morphological, Optical and Electrical Properties of Femtosecond Pulsed Laser Deposited TiO_2 Thin Films. *Sci. Rep.* **2020**, *10*, 10144. [CrossRef] [PubMed]
28. Singh, A.; Vihinen, J.; Frankberg, E.; Hyvärinen, L.; Honkanen, M.; Levänen, E. Pulsed Laser Ablation-Induced Green Synthesis of TiO_2 Nanoparticles and Application of Novel Small Angle X-Ray Scattering Technique for Nanoparticle Size and Size Distribution Analysis. *Nanoscale. Res. Lett.* **2016**, *11*, 447. [CrossRef]
29. Gupta, S.; Tripathi, M. A Review on the Synthesis of TiO_2 Nanoparticles by Solution Route. *Open Chem.* **2012**, *10*, 279–294. [CrossRef]
30. Chrisey, D.B.; Piqué, A.; McGill, R.A.; Horwitz, J.S.; Ringeisen, B.R.; Bubb, D.M.; Wu, P.K. Laser Deposition of Polymer and Biomaterial Films. *Chem. Rev.* **2003**, *103*, 553–576. [CrossRef]
31. Greer, J.A. Design Challenges for Matrix Assisted Pulsed Laser Evaporation and Infrared Resonant Laser Evaporation Equipment. *Appl. Phys. A* **2011**, *105*, 661–671. [CrossRef]
32. Datcu, A.; Duta, L.; Pérez del Pino, A.; Logofatu, C.; Luculescu, C.; Duta, A.; Perniu, D.; György, E. One-Step Preparation of Nitrogen Doped Titanium Oxide/Au/Reduced Graphene Oxide Composite Thin Films for Photocatalytic Applications. *RSC Adv.* **2015**, *5*, 49771–49779. [CrossRef]
33. Camps, I.; Borlaf, M.; Colomer, M.T.; Moreno, R.; Duta, L.; Nita, C.; Perez del Pino, A.; Logofatu, C.; Serna, R.; György, E. Structure-Property Relationships for Eu Doped TiO_2 Thin Films Grown by a Laser Assisted Technique from Colloidal Sols. *RSC Adv.* **2017**, *7*, 37643–37653. [CrossRef]
34. Cancea, V.N.; Ion, V.; Filipescu, M.; Stokker-Cheregi, F.; Dumitru, M.; Colceag, D.; Ionita, M.D.; Dinescu, M. Effect of Substrate Composition and Topography on the Improvement of Wettability of Titanium Dioxide Thin Films. *J. Optoelectron. Adv. Mater.* **2014**, *16*, 804–811.
35. Caricato, A.P.; Belviso, M.R.; Catalano, M.; Cesaria, M.; Cozzoli, P.D.; Luches, A.; Manera, M.G.; Martino, M.; Rella, R.; Taurino, A. Study of Titania Nanorod Films Deposited by Matrix-Assisted Pulsed Laser Evaporation as a Function of Laser Fluence. *Appl. Phys. A* **2011**, *105*, 605–610. [CrossRef]
36. Chen, X.; Mao, S.S. Titanium Dioxide Nanomaterials: Synthesis, Properties, Modifications, and Applications. *Chem. Rev.* **2007**, *107*, 2891–2959. [CrossRef]
37. Caputo, G.; Nobile, C.; Kipp, T.; Blasi, L.; Grillo, V.; Carlino, E.; Manna, L.; Cingolani, R.; Cozzoli, P.D.; Athanassiou, A. Reversible Wettability Changes in Colloidal TiO_2 Nanorod Thin-Film Coatings under Selective UV Laser Irradiation. *J. Phys. Chem. C* **2008**, *112*, 701–714. [CrossRef]
38. Li, L.; Li, G.; Xu, J.; Zheng, J.; Tong, W.; Hu, W. Insights into the Roles of Organic Coating in Tuning the Defect Chemistry of Monodisperse TiO_2 Nanocrystals for Tailored Properties. *Phys. Chem. Chem. Phys.* **2010**, *12*, 10857–10864. [CrossRef]
39. Sellinger, A.; Leveugle, E.; Fitz-Gerald, J.M.; Zhigilei, L.V. Generation of Surface Features in Films Deposited by Matrix-Assisted Pulsed Laser Evaporation: The Effects of the Stress Confinement and Droplet Landing Velocity. *Appl. Phys. A* **2008**, *92*, 821–829. [CrossRef]
40. Caricato, A.P.; Arima, V.; Cesaria, M.; Martino, M.; Tunno, T.; Rinaldi, R.; Zacheo, A. Solvent-Related Effects in MAPLE Mechanism. *Appl. Phys. B* **2013**, *113*, 463–471. [CrossRef]
41. Leveugle, E.; Zhigilei, L.V.; Sellinger, A.; Fitz-Gerald, J.M. Computational and Experimental Study of the Cluster Size Distribution in MAPLE. *Appl. Surf. Sci.* **2007**, *253*, 6456–6460. [CrossRef]
42. Zhou, J.; Man, X.; Jiang, Y.; Doi, M. Structure Formation in Soft-Matter Solutions Induced by Solvent Evaporation. *Adv. Mater.* **2017**, *29*, 1703769. [CrossRef]
43. Cozzoli, P.D.; Kornowski, A.; Weller, H. Low-Temperature Synthesis of Soluble and Processable Organic-Capped Anatase TiO_2 Nanorods. *J. Am. Chem. Soc.* **2003**, *125*, 14539–14548. [CrossRef]
44. Buonsanti, R.; Grillo, V.; Carlino, E.; Giannini, C.; Kipp, T.; Cingolani, R.; Cozzoli, P.D. Nonhydrolytic Synthesis of High-Quality Anisotropically Shaped Brookite TiO_2 Nanocrystals. *J. Am. Chem. Soc.* **2008**, *130*, 11223–11233. [CrossRef]
45. Piqué, A.; McGill, R.A.; Chrisey, D.B.; Leonhardt, D.; Mslna, T.E.; Spargo, B.J.; Callahan, J.H.; Vachet, R.W.; Chung, R.; Bucaro, M.A. Growth of Organic Thin Films by the Matrix Assisted Pulsed Laser Evaporation (MAPLE) Technique. *Thin Solid Film.* **1999**, *355–356*, 536–541. [CrossRef]
46. Thompson, T.L.; Yates, J.T. Surface Science Studies of the Photoactivation of TiO_2 New Photochemical Processes. *Chem. Rev.* **2006**, *106*, 4428–4453. [CrossRef] [PubMed]
47. Caputo, G.; Cingolani, R.; Cozzoli, P.D.; Athanassiou, A. Wettability Conversion of Colloidal TiO_2 Nanocrystal Thin Films with UV-Switchable Hydrophilicity. *Phys. Chem. Chem. Phys.* **2009**, *11*, 3692–3700. [CrossRef] [PubMed]
48. Caricato, A.P.; Luches, A.; Rella, R. Nanoparticle Thin Films for Gas Sensors Prepared by Matrix Assisted Pulsed Laser Evaporation. *Sensors* **2009**, *9*, 2682–2696. [CrossRef] [PubMed]
49. Leveugle, E.; Zhigilei, L.V. Molecular Dynamics Simulation Study of the Ejection and Transport of Polymer Molecules in Matrix-Assisted Pulsed Laser Evaporation. *J. Appl. Phys.* **2007**, *102*, 074914. [CrossRef]

50. Deng, Y.; Ma, Z.; Ren, F.; Wang, G. Enhanced Photoelectrochemical Performance of TiO_2 Nanorod Array Films Based on TiO_2 Compact Layers Synthesized by a Two-Step Method. *RSC Adv.* **2019**, *9*, 21777–21785. [CrossRef]
51. Liu, T.; Luo, H.; Ma, J.; Xie, W.; Wang, Y.; Jing, G. Surface Roughness Induced Cracks of the Deposition Film from Drying Colloidal Suspension. *Eur. Phys. J. E* **2016**, *39*, 24. [CrossRef]
52. Bubb, D.M.; Corgan, J.; Yi, S.; Khan, M.; Hughes, L.; Gurudas, U.; Papantonakis, M.; McGill, R.A. An Experimental Investigation of Inhomogeneities in Resonant Infrared Matrix-Assisted Pulsed-Laser Deposited Thin Polymer Films. *Appl. Phys. A* **2010**, *100*, 523–531. [CrossRef]
53. Feng, E.Y.; Zelaya, R.; Holm, A.; Yang, A.-C.; Cargnello, M. Investigation of the Optical Properties of Uniform Platinum, Palladium, and Nickel Nanocrystals Enables Direct Measurements of Their Concentrations in Solution. *Colloids Surf. A Physicochem. Eng. Asp.* **2020**, *601*, 125007. [CrossRef]
54. Vidal-Vidal, J.; Rivas, J.; López-Quintela, M.A. Synthesis of Monodisperse Maghemite Nanoparticles by the Microemulsion Method. *Colloids Surf. A Physicochem. Eng. Asp.* **2006**, *288*, 44–51. [CrossRef]
55. Patra, N.; Salerno, M.; Malerba, M.; Cozzoli, P.D.; Athanassiou, A. Improvement of Thermal Stability of Poly(Methyl Methacrylate) by Incorporation of Colloidal TiO_2 Nanorods. *Polym. Degrad. Stab.* **2011**, *96*, 1377–1381. [CrossRef]
56. Belman, N.; Israelachvili, J.N.; Li, Y.; Safinya, C.R.; Ezersky, V.; Rabkin, A.; Sima, O.; Golan, Y. Hierarchical Superstructure of Alkylamine-Coated ZnS Nanoparticle Assemblies. *Phys. Chem. Chem. Phys.* **2011**, *13*, 4974–4979. [CrossRef] [PubMed]
57. Mehta, S.K.; Kumar, S.; Chaudhary, S.; Bhasin, K.K. Nucleation and Growth of Surfactant-Passivated CdS and HgS Nanoparticles: Time-Dependent Absorption and Luminescence Profiles. *Nanoscale* **2010**, *2*, 145–152. [CrossRef] [PubMed]
58. Mariano, F.; Caricato, A.P.; Accorsi, G.; Leo, C.; Cesaria, M.; Carallo, S.; Genco, A.; Simeone, D.; Tunno, T.; Martino, M.; et al. White Multi-Layered Polymer Light Emitting Diode through Matrix Assisted Pulsed Laser Evaporation. *J. Mater. Chem. C* **2016**, *4*, 7667–7674. [CrossRef]
59. Rodrigo, K.; Czuba, P.; Toftmann, B.; Schou, J.; Pedrys, R. Surface Morphology of Polyethylene Glycol Films Produced by Matrix-Assisted Pulsed Laser Evaporation (MAPLE): Dependence on Substrate Temperature. *Appl. Surf. Sci.* **2006**, *252*, 4824–4828. [CrossRef]
60. Worthington, A.M.; Clifton, R.B. XXVIII. On the Forms Assumed by Drops of Liquids Falling Vertically on a Horizontal Plate. *Proc. R. Soc. Lond.* **1877**, *25*, 261–272. [CrossRef]
61. Yarin, A.L. DROP IMPACT DYNAMICS: Splashing, Spreading, Receding, Bouncing. . .. *Annu. Rev. Fluid Mech.* **2006**, *38*, 159–192. [CrossRef]
62. Thoroddsen, S.T.; Etoh, T.G.; Takehara, K. High-Speed Imaging of Drops and Bubbles. *Annu. Rev. Fluid Mech.* **2008**, *40*, 257–285. [CrossRef]
63. Josserand, C.; Thoroddsen, S.T. Drop Impact on a Solid Surface. *Annu. Rev. Fluid Mech.* **2016**, *48*, 365–391. [CrossRef]
64. Hao, J. Effect of Surface Roughness on Droplet Splashing. *Phys. Fluids* **2017**, *29*, 122105. [CrossRef]
65. Xu, L. Liquid Drop Splashing on Smooth, Rough, and Textured Surfaces. *Phys. Rev. E* **2007**, *75*, 056316. [CrossRef] [PubMed]
66. Tang, C.; Qin, M.; Weng, X.; Zhang, X.; Zhang, P.; Li, J.; Huang, Z. Dynamics of Droplet Impact on Solid Surface with Different Roughness. *Int. J. Multiph. Flow* **2017**, *96*, 56–69. [CrossRef]
67. Tsai, P.; CA van der Veen, R.; van de Raa, M.; Lohse, D. How Micropatterns and Air Pressure Affect Splashing on Surfaces. *Langmuir* **2010**, *26*, 16090–16095. [CrossRef]
68. Li, W.; Bai, Y.; Liu, C.; Yang, Z.; Feng, X.; Lu, X.; van der Laak, N.K.; Chan, K.-Y. Highly Thermal Stable and Highly Crystalline Anatase TiO_2 for Photocatalysis. *Environ. Sci. Technol.* **2009**, *43*, 5423–5428. [CrossRef]
69. Hanaor, D.A.H.; Sorrell, C.C. Review of the Anatase to Rutile Phase Transformation. *J. Mater. Sci.* **2011**, *46*, 855–874. [CrossRef]
70. Chen, X.; Hosseini, S.N.; van Huis, M.A. Heating-Induced Transformation of Anatase TiO_2 Nanorods into Rock-Salt TiO Nanoparticles: Implications for Photocatalytic and Gas-Sensing Applications. *ACS Appl. Nano Mater.* **2022**, *5*, 1600–1606. [CrossRef]
71. Perego, C.; Revel, R.; Durupthy, O.; Cassaignon, S.; Jolivet, J.-P. Thermal Stability of TiO_2-Anatase: Impact of Nanoparticles Morphology on Kinetic Phase Transformation. *Solid State Sci.* **2010**, *12*, 989–995. [CrossRef]
72. Vásquez, G.C.; Peche-Herrero, M.A.; Maestre, D.; Gianoncelli, A.; Ramírez-Castellanos, J.; Cremades, A.; González-Calbet, J.M.; Piqueras, J. Laser-Induced Anatase-to-Rutile Transition in TiO_2 Nanoparticles: Promotion and Inhibition Effects by Fe and Al Doping and Achievement of Micropatterning. *J. Phys. Chem. C* **2015**, *119*, 11965–11974. [CrossRef]
73. Gribb, A.A.; Banfield, J.F. Particle Size Effects on Transformation Kinetics and Phase Stability in Nanocrystalline TiO_2. *Am. Mineral.* **1997**, *82*, 717–728. [CrossRef]
74. Zhang, H.; Banfield, J.F. Understanding Polymorphic Phase Transformation Behavior during Growth of Nanocrystalline Aggregates: Insights from TiO_2. *J. Phys. Chem. B* **2000**, *104*, 3481–3487. [CrossRef]
75. Guisbiers, G.; Van Overschelde, O.; Wautelet, M. Theoretical Investigation of Size and Shape Effects on the Melting Temperature and Energy Bandgap of TiO_2 Nanostructures. *Appl. Phys. Lett.* **2008**, *92*, 103121. [CrossRef]
76. Cozzoli, P.D.; Comparelli, R.; Fanizza, E.; Curri, M.L.; Agostiano, A. Photocatalytic Activity of Organic-Capped Anatase TiO_2 Nanocrystals in Homogeneous Organic Solutions. *Mater. Sci. Eng. C* **2003**, *23*, 707–713. [CrossRef]

77. György, E.; Pérez del Pino, Á.; Roqueta, J.; Ballesteros, B.; Cabana, L.; Tobias, G. Effect of Laser Radiation on Multi-Wall Carbon Nanotubes: Study of Shell Structure and Immobilization Process. *J. Nanoparticle Res.* **2013**, *15*, 1852. [CrossRef]
78. Del Pino, Á.P.; György, E.; Cabana, L.; Ballesteros, B.; Tobias, G. Deposition of Functionalized Single Wall Carbon Nanotubes through Matrix Assisted Pulsed Laser Evaporation. *Carbon* **2012**, *50*, 4450–4458. [CrossRef]
79. Jeong, J.; Sekiguchi, K.; Sakamoto, K. Photochemical and Photocatalytic Degradation of Gaseous Toluene Using Short-Wavelength UV Irradiation with TiO_2 Catalyst: Comparison of Three UV Sources. *Chemosphere* **2004**, *57*, 663–671. [CrossRef]